Dynamics of nuclear single-particle structure in covariant theory of particle-vibration coupling: From light to superheavy nuclei

E. V. Litvinova
GSI Helmholtzzentrum für Schwerionenforschung, D-64291 Darmstadt, Germany and
Institut für Theoretische Physik, Goethe-Universität, D-60438 Frankfurt am Main, Germany

A. V. Afanasjev
Department of Physics and Astronomy, Mississippi State University, Mississippi 39762, USA
(Received 26 March 2011; published 7 July 2011)

The impact of particle-vibration coupling and polarization effects due to deformation and time-odd mean fields on single-particle spectra is studied systematically in doubly magic nuclei from low-mass ^{56}Ni up to superheavy ones. Particle-vibration coupling is treated fully self-consistently within the framework of the relativistic particle-vibration coupling model. Polarization effects due to deformation and time-odd mean field induced by odd particle are computed within covariant density functional theory. It has been found that among these contributions the coupling to vibrations makes a major impact on the single-particle structure. The impact of particle-vibration coupling and polarization effects on calculated single-particle spectra, the size of the shell gaps, the spin-orbit splittings and the energy splittings in pseudospin doublets is discussed in detail; these physical observables are compared with experiment. Particle-vibration coupling has to be taken into account when model calculations are compared with experiment since this coupling is responsible for observed fragmentation of experimental levels; experimental spectroscopic factors are reasonably well described in model calculations.

DOI: 10.1103/PhysRevC.84.014305 PACS number(s): 21.10.Pc, 21.10.Re, 21.60.Jz, 27.90.+b

I. INTRODUCTION

The covariant density functional theory (CDFT) [1–3] is one of standard tools of nuclear theory which offers considerable potential for further development. Built on Lorentz covariance and the Dirac equation, it provides a natural incorporation of spin degrees of freedom [1,2] and an accurate description of spin-orbit splittings [2] (see also Fig. 2 in Ref. [4]), which has an essential influence on the underlying shell structure. Note that the spin-orbit interaction is a relativistic effect, which arises naturally in the CDFT theory. Lorentz covariance of the CDFT equations leads to the fact that time-odd mean fields of this theory are determined as spatial components of Lorentz vectors and therefore coupled with the same constants as time-like components [5] which are fitted to ground-state properties of finite nuclei. In addition, pseudo-spin symmetry finds a natural explanation in the relativistic framework [6]. CDFT in its different incarnations both on the mean-field and beyond mean-field levels provides successful description of many properties of ground-state and excited configurations in nuclei [3].

However, the majority of applications of CDFT have been focused on collective properties of nuclei. There are only few features on nuclear systems, strongly dependent on single-particle degrees of freedom, which have been addressed in the CDFT studies on the mean-field level and compared with experiment. These are the single-particle properties in spherical and deformed nuclei, spin-orbit splittings in spherical nuclei, magnetic moments in the $A \pm 1$ neighbours of the ^{16}O nucleus ($A = 16$) [7], and alignment properties of single-particle orbitals in rotating nuclei [8].[1]

The calculated single-particle spectra of spherical nuclei are frequently compared with experiment (see, for example, Refs. [1,2]). However, only in Refs. [4,13] are deformation polarization effects and time-odd mean fields included in the calculations, which makes them more realistic. The spin-orbit splittings, as extracted from the single-particle energies obtained in spherical CDFT calculations, reproduce the experimental spin-orbit splittings fairly well, although there are deviations up to 20% of absolute value of the splitting (see Figs. 11, 12 and Table IV in Ref. [13] and Fig. 2 and Sect. IV B in Ref. [4]) which only weakly depend on the relativistic mean-field (RMF) parametrization. Note that the comparison of Ref. [4] includes the uncertainty of the spin-orbit splittings due to deformation polarization effects and time-odd mean fields as they are found in Ref. [13]. Ref. [4] clearly shows that spin-orbit splittings are better described in CDFT as compared with Skyrme energy density functional theory (SEDFT) despite the fact that no single-particle information (contrary to SEDFT) has been used in the fit of the RMF Lagrangian.

These comparisons, however, do not reveal the accuracy of the description of the single-particle states because the particle-vibration coupling (PVC), which can affect considerably the energies of single-particle states in odd-mass nuclei [14–18],

[1]Effective alignments of compared rotational bands, which depend sensitively on both the alignment properties of single-particle orbital by which two bands differ and polarization effects induced by the particle in this orbital, are in average better reproduced in the CDFT calculations than in the cranked Nilsson-Strutinsky calculations based on phenomenological Nilsson potential, see comparisons presented in Refs. [9–11]. This is despite the fact that no single-particle information has been used in the fit of the CDFT parameters, while the parameters of the Nilsson potential are fitted to experimental single-particle energies (see Ref. [12]).

has been neglected. The modification of the quasiparticle states by particle-vibration coupling is weaker in deformed nuclei [19,20] since the surface vibrations are more fragmented (less collective) than in spherical nuclei [19,21]. As a consequence, the corrections to the energies of quasiparticle states in odd nuclei due to particle-vibration coupling are expected to be less state-dependent in deformed nuclei. Hence the comparison between experimental and calculated energies of single-particle states is expected to be less ambiguous in deformed nuclei as compared with spherical ones [16,21], at least at low excitation energies, where vibrational admixtures in the wave functions are small. The analysis of the energies of one-quasiparticle deformed states in the actinide region, performed within the relativistic Hartree-Bogoliubov (RHB) approach in Refs. [22,23], reveals that while the majority of the states are described with an accuracy better than 0.5 MeV, there are a number of states which deviate from experiment by as much as 1 MeV.

The question arises of which features of the DFT are most decisive for the single-particle structure. The most crucial ingredients in this respect are:

(i) the effective nucleon mass and its radial dependence, which determines the level density near the Fermi surface. It is well known that the one-(quasi-)particle spectra calculated on the mean-field level are less dense than in experiment both at spherical [14–17] and deformed [22,23] shapes. The average level density of the single-particle states on the mean-field level is related to the effective mass (Lorentz mass in the notation of Ref. [24] for the case of CDFT theory) of the nucleons at the Fermi surface: $m^*_L(k_F)/m$. The CDFT is characterized by a low effective mass $m^*_L(k_F)/m \approx 0.66$ [4]. As a consequence, this low effective mass of CDFT has a bigger impact on the single-particle spectra than the effective masses of nonrelativistic DFT which are typically larger. Note that at spherical shape the inclusion of particle-vibrational coupling brings the calculated level density closer to the experimental one characterized by an effective mass $m^*(k_F)/m \approx 1.0$ [17].

(ii) the spin-orbit potential, which determines the energetic distance of the spin-orbit partners. It is well known that CDFT describes rather well spin-orbit splittings [4]. However, these results have been obtained on the mean-field level, and it is necessary to test how they will be affected by the inclusion of particle-vibrational coupling. In CDFT theory the Dirac effective mass $m^*_D(k_F)/m$ is closely related to the effective spin-orbit single-nucleon potential, and empirical energy spacings between spin-orbit partner states in finite nuclei determine a relatively narrow interval of allowed values: $0.57 \leqslant m^*_D(k_F)/m \leqslant 0.61$ [25]. This requirement restricts considerably the possible parametrizations of the RMF Lagrangian on the mean-field level, and thus it would be interesting to see whether the inclusion of PVC will loosen this requirement and thus allow a wider range of effective masses in the CDFT.

(iii) the density dependence of the effective potential and effective mass, which has an influence on the relative position of the states with different orbital angular momentum l. The investigation of Ref. [13], covering spherical odd nuclei bordering doubly magic nuclei clearly showed that the relative placement of the states with different orbital angular momenta l is not so well reproduced on the mean-field level in CDFT. The problems occur predominantly in connection with the states of high l which hints that the surface profile of the mean-field and kinetic terms are involved. Microscopic consideration in many-body theory indicates that the effective mass has a pronounced surface profile which is insufficiently parametrized in the present mean-field models [16]. Thus, it is important to see whether the inclusion of PVC will improve the description of the relative positions of the states with different orbital angular momentum l.

In Ref. [17], a relativistic particle-vibration coupling model has been developed and the calculations based on the NL3 [26] parametrization of the CDFT have been performed for the doubly magic ^{208}Pb nucleus. In this work we present a more systematic investigation within this model including the calculations covering the nuclei from light ^{56}Ni and medium-mass ^{100}Sn and ^{132}Sn to heavy ^{208}Pb and superheavy ^{292}120 doubly magic nuclei using improved (as compared with NL3) NL3* [27] parametrization of the CDFT. This investigation covers neutron-deficient near-proton-drip-line nuclei (^{56}Ni and ^{100}Sn), the neutron-rich ^{132}Sn nucleus, and the ^{208}Pb nucleus located at the beta-stability line. In addition, the polarization effects in odd-mass nuclei due to deformation and time-odd mean fields are treated by means of cranked relativistic mean-field (CRMF) calculations.

The article is organized as follows: The method of comparison of experimental and theoretical single-particle levels is discussed in Sec. II. Section III presents relativistic particle-vibration model and cranked relativistic mean-field theory and their details related to the study of single-particle states. The comparison of model calculations with experiment is presented in Sec. IV. The accuracy of the description of single-particle spectra and spectroscopic factors, the impact of particle-vibration coupling on shell gaps, spin-orbit splittings, and pseudospin doublets as well as the role of polarization effects in odd-mass nuclei due to deformation and time-odd mean fields are discussed in detail. Finally, Sec. V reports the main conclusions of our work.

II. EXPERIMENTAL VERSUS THEORETICAL SINGLE-PARTICLE ENERGIES

The experimental information about single-particle level structure of even-even doubly magic nucleus with the proton number Z_0 and neutron number N_0 originates from the odd-mass $(Z_0 \pm 1)$ and $(N_0 \pm 1)$ nuclear neighbors. In odd-mass nuclei, the polarization effects due to deformation

and time-odd (TO) mean fields[2] induced by odd particles play an important role (see Sec. IV B). In addition, the particle-vibration coupling modifies the energies and the structure of the levels (Secs. IV C and IV E); neither of them remains purely single-particle in nature. In order to describe all these effects we use a hybrid model (labelled as "hybrid" below), in which the polarization effects due to deformation and TO mean fields are treated on the mean-field level within the cranked relativistic mean-field (CRMF) approach (see Sec. III A), while the corrections due to the PVC are treated within the relativistic particle-vibration coupling model (see Sec. III B). The need for such a hybrid model is dictated by the fact that the PVC model is not variational in nature and thus it does not allow the calculation of polarization effects due to odd particle. Since the polarization effects and the corrections due to the PVC have a different origin, they are treated as additive quantities in the hybrid model which is a reasonable approximation. The details of the hybrid model are discussed in Sec. III.

The experimental and calculated energies of the particle [ε(particle)] and hole [ε(hole)] states closest to the Fermi level are determined from the difference of the binding energies of the core [B(core)] and the corresponding adjacent odd nuclei [B(core + nucleon) and B(core − nucleon)] as [13,29]

$$\varepsilon(\text{particle}) = B(\text{core}) - B(\text{core} + \text{nucleon}) \tag{1}$$

and

$$\varepsilon(\text{hole}) = B(\text{core} - \text{nucleon}) - B(\text{core}). \tag{2}$$

These quantities correspond to one-particle removal energies. We will refer to them as single-particle energies to simplify the discussion. Doubly magic spherical nuclei ^{56}Ni, ^{100,132}Sn, and ^{208}Pb are used as the cores in our analysis. Their ground states are not affected by PVC. The experimental energies of particle and hole defined according to these equations include the polarization effects due to deformation and TO mean fields induced by odd particle or hole as well as the energy corrections due to particle-vibration coupling in odd-mass nuclei. Thus, their comparison with the results of "hybrid" calculations is straightforward.

On the other hand, there are some unresolved questions when these energies are compared with pure mean-field calculations as it is done frequently in the literature. The problem is related to the fact that experimental single-particle levels and their energies and structure are affected by the particle-vibration coupling which is neglected on the mean-field level. Each mean-field state k with energy ε_k is split into many levels due to particle-vibration coupling, so the single-particle strength is fragmented over many levels. In the diagonal approximation for the nucleonic self-energy, these levels have the same quantum numbers as the original mean-field state k, but different energies ε_k^ν and spectroscopic factors S_k^ν. Unlike the Hartree or Hartree-Fock approximations without pairing where the single-particle states are either fully occupied or empty, in the PVC model their occupation probabilities are the real numbers between zero and one, so that the sum rule

$$\sum_\nu S_k^\nu = 1 \tag{3}$$

is satisfied. For the states in the vicinity of the Fermi surface one usually obtains one dominant level with $0.5 \leqslant S_k^\nu \leqslant 1.0$ and many other levels with small S_k^ν. For the states far from the Fermi surface one observes very strong splitting over many levels with much smaller and comparable spectroscopic factors; see the detailed analysis in Ref. [17] for ^{208}Pb.

This discussion clearly indicates that some procedure has to be employed in order to extract pure (or "bare") single-particle energies from experimental data which have to be compared with mean-field single-particle energies ε_k. Two such procedures have been discussed in the literature.

In the first procedure, the energy of the dominant fragment is corrected by the energy shift due to particle-vibration coupling leading to a "bare" single-particle energy. Such energies of the doubly magic nuclei are extracted in some publications; see, for example, Ref. [30]. However, this procedure relies on the choice of particle-vibration coupling model. However, different PVC models lead to different energy shifts (see Table I in Ref. [31]). In addition, such a procedure frequently neglects polarization effects due to deformation and TO mean fields which are again model dependent. For example, there is no time-odd mean fields in the phenomenological models based on the Nilsson or Woods-Saxon potentials.

In the second procedure, the center of gravity of the fragmented levels with a given quantum number j^π (j is the total angular momentum and π is a parity) and energies ε_k^ν is obtained via the weighted-average [32,33] procedure

$$\varepsilon_k^{\text{grav}} = \left[\sum_\nu S_k^\nu \varepsilon_k^\nu\right] \Big/ \left[\sum_\nu S_k^\nu\right]. \tag{4}$$

This energy is then associated with a "bare" single-particle energy. This expression is fulfilled exactly in the PVC model discussed in Sec. III B and it is satisfied with high accuracy in this model numerical implementation. The normalization in this procedure (which is omitted in some publications) is used to minimize the uncertainties due to large experimental errors in spectroscopic factors, since these errors lead to the fact that the sum rule $\sum_\nu S_k^\nu = 1$ is poorly fulfilled in the majority of experiments. The application of this procedure requires that all ν levels to which the single-particle state k is fragmented are identified in the experiment and that spectroscopic factors are measured accurately. These conditions are definitely not satisfied in the ^{56}Ni and ^{100,132}Sn nuclei.

The situation is somewhat better in ^{208}Pb, for which the $\varepsilon_k^{\text{grav}}$ values have been extracted in Ref. [33] for a number of levels. However, even in this case the accuracy of the definition of $\varepsilon_k^{\text{grav}}$ is not known because of the number of reasons listed below. The absolute values of spectroscopic factors are characterized by large ambiguities and depend strongly on the reaction employed in experiment and the reaction model used in the analysis [33,34]. The spectroscopic factors in odd-mass nuclei have been obtained in different reactions;

[2]The name "nuclear magnetism" is frequently used in the CDFT to describe the effect of time-odd mean fields induced by the magnetic potential of the Dirac equation since this potential has the structure of a magnetic field [5,28].

TABLE I. Average deviations per state $\Delta\varepsilon$ between calculated and experimental energies of the single-particle states for a proton (neutron) subsystem of a given nucleus. The results obtained in the "def + TO" and "hybrid" calculational schemes are shown.

Nucleus/Subsystem	$\Delta\varepsilon_{\text{def+TO}}$ [MeV]	$\Delta\varepsilon_{\text{hybrid}}$ [MeV]
^{56}Ni/proton	0.76	0.77
^{56}Ni/neutron	0.89	0.71
^{132}Sn/proton	1.02	0.68
^{132}Sn/neutron	0.89	0.39
^{208}Pb/proton	1.53	0.84
^{208}Pb/neutron	1.00	0.47

for example, in the $(d,^3\text{He})$ reaction for ^{207}Tl [35], (α, t) for ^{209}Bi [36], $(^3\text{He},\alpha)$ [37] and (d,t) [38] for ^{207}Pb. Even in the same nucleus different reactions give different spectroscopic factors (see, for example, Table I in Ref. [38] and Table III in the current manuscript). In addition, the spins and parities of many high-lying fragments are uncertain (see, for example, Table I in Ref. [35]) and/or only the part of the sum rule strength has been observed in experiment (see, for example, Ref. [36]). As a consequence, it is not clear whether the complete set of the ν levels to which the single-particle state k is fragmented and their spectroscopic factors have been identified in experiment.

In the light of this discussion it is clear that "bare" single-particle energies cannot be defined with controllable precision in the nuclei under study. As a result, we compare observed experimental levels directly with mean-field calculations. Such an approach is frequently used in the literature (see, for example, Refs. [2,13,29]). It has clear limitations, but at least it allows us to see (i) whether the inclusion of particle-vibration coupling improves the description of specific physical observables and (ii) whether or not the conclusions reached earlier on the mean-field level are valid.

III. THEORETICAL FRAMEWORK

A. Mean-field level: Polarization effects

Mean-field results related to polarization effects due to deformation and TO mean fields in odd-mass nuclei have been obtained using cranked relativistic mean-field (CRMF) theory [28,39,40]. Although this theory was initially developed for the description of rotating nuclei, it is also able to describe the nuclear systems with broken time-reversal symmetry in an intrinsic frame at no rotation in which TO mean fields play an important role (see Ref. [5]).

The application of the CRMF theory has the following advantages. First, the CRMF computer code is formulated in the signature basis. As a result, the breaking of Kramer's degeneracy of the single-particle states in odd-mass nuclei is taken into account in a fully self-consistent way. This is important for an accurate description of TO mean fields (Ref. [5]). These fields have considerable impact on the moments of inertia in rotating nuclei [41] and the fact that the properties of such nuclei are well described in the CRMF code (see Refs. [3,41]) adds confidence to proper description of TO mean fields in nonrotating systems [5]. Second, the CRMF computer code is formulated in three-dimensional cartesian coordinates which allows us to describe not only axially deformed but also triaxial nuclear shapes. This is important for a proper description of polarization effects due to deformation.

It is a well-known fact that the description of pairing correlations in doubly magic nuclei and their close neighborhood is notoriously difficult and model-dependent (Ref. [42]). The presence of large shell gaps leads to a pairing collapse in the models with the treatment of pairing on the BCS or Hartree-Fock-Bogoliubov (HFB) levels. This is seen, for example, in nonrelativistic HFB calculations with the Gogny D1S force of ^{100,132}Sn in Ref. [42]. The calculations within the relativistic Hartree-Bogoliubov (RHB) framework of Ref. [43] with the same force for pairing also show pairing collapse in the ground states of ^{56}Ni, ^{100,132}Sn, and ^{208}Pb. The pairing correlations are restored when the particle-number projection is implemented. However, there is a substantial difference between different approaches [such as the Lipkin-Nogami (LN) method of approximate particle-number projection or projection after variation (PAV) approach] and the variation after projection (VAP) approach; the latter represents the best approach for the treatment of pairing correlations [15]. The RHB + LN calculations with the Gogny D1S force for pairing show very weak pairing in the nuclei of interest. The additional binding due to pairing (relatively to the results with no pairing) is only 0.333 MeV, 0.284 MeV, 0.493 MeV, and 0.557 MeV in ^{56}Ni, ^{100,132}Sn, and ^{208}Pb, respectively. The blocking of a single-particle orbital in an odd-mass nucleus leads to the weakening of pairing correlations and to frequent unphysical pairing collapse even in the RHB + LN calculations. The physical quantities, such as given by Eqs. (1) and (2), are relative in nature. Thus, we believe that in the case of weak pairing they are sufficiently well described in unpaired calculations. As a consequence, we neglect pairing correlations in the CRMF calculations. Note that they are also neglected in the PVC calculations.

Similar to Ref. [13], binding energies of odd-A nuclei were calculated by blocking the $(n_r + 1, j^\pi, j)$ state [amongst the $(n_r + 1, j^\pi, m)$ states] with the largest projection $m = j$ onto the symmetry axis. Here, the n_r and j are the single-nucleon radial and total angular momentum quantum numbers. The spherical subshell label of this state is used to label the configuration of the odd-mass nucleus since the deformations (induced by the odd particle or hole) of immediate odd-A neighbors of doubly magic nuclei are rather small.

B. Beyond covariant density functional theory: Single-particle spectra of nuclei

1. Particle-vibration coupling model of time dependence of nucleonic self-energy

The mean-field approach, being a very useful and convenient theoretical tool to describe finite nuclei, is, however, only a static and local approximation to the many-body problem. The nonlocality (or, equivalently, momentum dependence) is implicitly taken into account by an effective mass which is considerably smaller than the bare nucleon mass. This enables

one to reproduce reasonably well the general properties of the single-particle motion in the nuclear potential well. However, the mean-field approximations based on the widely used Skyrme, Gogny, as well as covariant density functionals generate excessively stretched single-particle spectra around the Fermi surface and often fail to describe the sequence of the single-particle levels. Proper inclusion of the time dependence in the nucleonic potential requires going beyond the mean-field description, which is static by construction.

The underlying physics responsible for the time dependence is related to many-body correlations; that is, to the part of the Hamiltonian which cannot be expressed in terms of the one-body density. In the medium-mass and heavy nuclei, the leading-order contribution of such correlations to the nucleonic self-energy comes from coupling of the nucleonic motion to the surface and volume vibrational modes (phonons). The most important collective vibrational modes are generated by the nuclear oscillations of coherent nature. Taking into account the coupling of these modes to the single-particle motion, the shell model acquires a dynamic content. These surface and volume oscillations, especially their low-lying modes, modify considerably the picture of the single-particle motion in nuclei. The main assumption of the quasiparticle-phonon coupling model is that two types of elementary degrees of freedom—one-quasiparticle (1-qp) and collective ones—are coupled in such a way that configurations of 1-qp⊗phonon type with low-lying phonons strongly compete with simple 1-qp configurations located close in energy or, in other words, that quasiparticles can emit and absorb phonons with rather high probabilities [44,45].

Taking the quasiparticle-phonon coupling into account as an additional time-dependent part of the nucleonic self-energy leads to the splitting of each mean-field single-particle state into many energy levels. The dominant levels (i.e., the levels with the largest spectroscopic factors) shift, as a rule, toward the Fermi level, improving considerably the agreement with data (see the review of various applications in Ref. [16] and references therein). This result is obtained, however, only for states within about 10 MeV of the Fermi energy. For the states lying far from the Fermi surface one observes a very strong fragmentation, making extraction of the dominant levels impossible.

A similar general picture has been obtained within the particle-vibration coupling extension of the covariant density functional theory [17]. Unlike the nonrelativistic versions of the model, in the extended CDFT the particle-phonon coupling self-energy allows intermediate nucleonic propagation through the Dirac sea states with negative energies, in addition to the particle and hole states in the Fermi sea. The contribution of the Dirac-sea terms to the self-energy at the Fermi level are, however, found to be negligibly small due to their large energy denominators.

2. Approximations

In the present investigation we retain basically the calculational scheme of Ref. [17]. This approach implies a linearized version of the particle-vibration coupling model: the Dyson equation for single-particle Green function contains the phonon-coupling self-energy with mean-field intermediate nucleonic propagators and phonon energies and vertices computed within the relativistic random phase approximation (RRPA) [46]. For medium-mass and heavy nuclei the RRPA gives a very reasonable description of the phonon spectra. Although a more precise description of the phonons can be achieved within an approach like the relativistic time-blocking approximation (RTBA) [47], particle-vibration coupling model of Ref. [17] by using the RRPA phonons takes into account the major contribution of the vibrational motion to the single-particle spectra.

The application of the model to the lightest doubly magic nuclei ^{16}O, ^{40}Ca, and ^{48}Ca requires, however, a special consideration because their mean-field single-particle level densities are too small to provide sizable configuration mixing around the Fermi surface. For ^{16}O and ^{40}Ca, it is not possible, in principle, to reproduce within the RRPA the low-lying phonons with positive parity (first positive parity particle-hole excitations are at excessively high energies). In such cases the phonon spectra for the nucleonic self-energy should be calculated, allowing an extension for coupling to more complex configurations; this implies a generalized particle-vibration coupling model and will be done in a separate work. In ^{48}Ca we have obtained a rather reasonable phonon spectrum, but the strong fragmentation of the hole states does not allow extraction of the dominant single-particle levels.

The phonons of unnatural parities are known to play only a marginal role in the nucleonic self-energy, so they are not included into the phonon space. Moreover, the inclusion of pairing vibrations into the phonon space has not yet been studied within the relativistic framework. In principle, they may bring some additional corrections to the results, although our approximation is justified by the results of Refs. [47,48], where the fragmentation of the collective modes has been reproduced very well without inclusion of the pairing vibrations.

C. Numerical details of calculations

The CRMF equations are solved in the basis of an anisotropic three-dimensional harmonic oscillator in Cartesian coordinates characterized by the deformation parameters $\beta_0 = 0.0$ and $\gamma = 0^\circ$ as well as the oscillator frequency $\hbar\omega_0 = 41A^{-1/3}$ MeV. The truncation of the basis is performed in such a way that all states belonging to the shells up to fermionic $N_F = 20$ and bosonic $N_B = 20$ are taken into account in the calculations. Numerical analysis indicates that this truncation scheme provides sufficient numerical accuracy for the physical quantities of interest. Note that the same truncation of basis is used in the RRPA and PVC calculations, but they are performed at spherical shape.

The NL3* [27] parametrization of the RMF Lagrangian is used in the CRMF, RRPA, and PVC calculations. This recently fitted parametrization has been successfully applied to the description of binding energies [27], ground-state properties of deformed nuclei [49], fission barriers [50], rotating nuclei [27], giant resonances [27], and breathing mode [51].

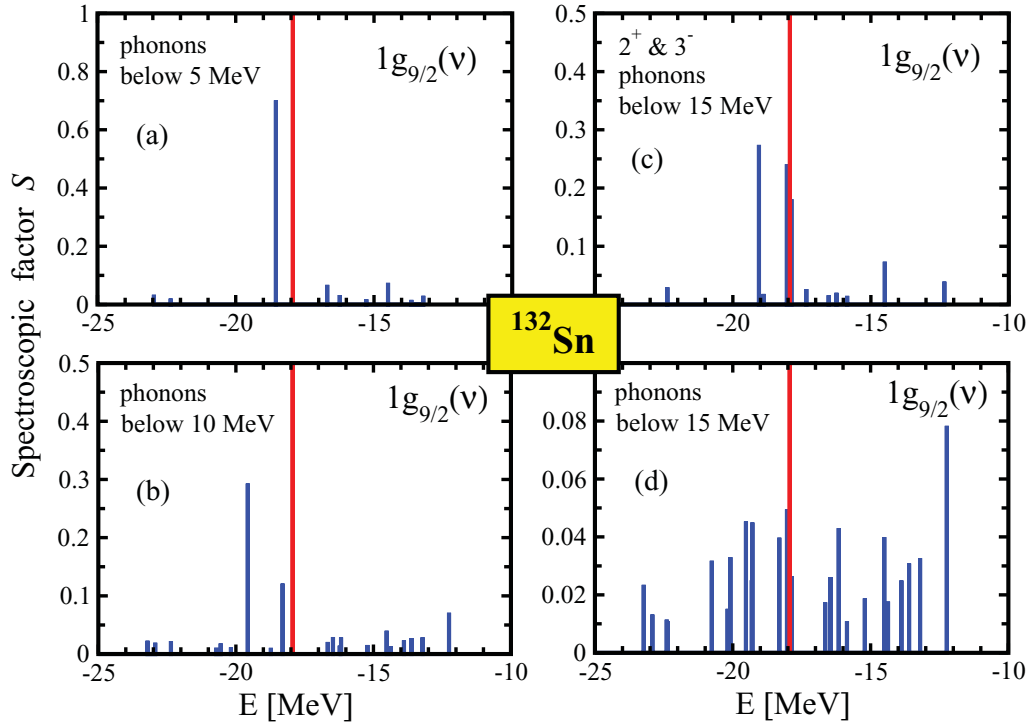

FIG. 1. (Color online) Single-particle strength distributions of the neutron $1g_{9/2}$ state in ^{132}Sn calculated within the PVC model with different numbers of the phonon modes. Red bars show the initial mean-field $1g_{9/2}$ neutron state.

D. Cutoff problem of phonon basis

Phonons of the multipolarities 2^+, 3^-, 4^+, 5^-, 6^+ with energies below 15 MeV are included in the model space of the PVC calculations. We have neglected only phonon modes with very small transition probabilities; less than 5% of the maximal ones for each J^π. The phonon energies and their coupling vertices have been computed within the self-consistent RRPA.

A rather good convergence of the phonon coupling self-energy with extension of the phonon space has been obtained numerically: with very few exceptions, the addition of phonon modes with energies above 15 MeV does not affect the results. Partial contributions from phonons with low angular momenta and low energies have been also investigated. An example of such a study is shown in Fig. 1 for the neutron $1g_{9/2}$ state in ^{132}Sn. This typical deeply bound hole state is strongly fragmented when the PVC is taken into account; see the panel (d) with the results obtained with the full phonon set below 15 MeV.

Panels (a) and (b) show the results obtained when only the phonons below 5 and 10 MeV, respectively, are taken into account. One can see that, in the former case, the picture is very different from that displayed in panel (d). In the latter case the results are already close to saturation, but there are still two states between -20 and -18 MeV with spectroscopic factors larger than 0.1. Panel (c) shows how the angular momentum cutoff weakens the fragmentation effect. A similar conclusion can be drawn for other states either far from or around the Fermi surface: cutoff of the angular momenta and of the phonon energies has to be made with care.

IV. RESULTS AND DISCUSSION

A. Theoretical and experimental spectra

An example of the comparison of the results of calculations and experiment is shown in Fig. 2. Column "sph" shows single-particle spectra obtained in spherical RMF calculations of even-even ^{56}Ni nucleus. Column "def" displays one-nucleon separation energies [defined according to Eqs. (1) and (2)] obtained in triaxial CRMF calculations in which only deformation polarization effects are taken into account. It is seen that these energies are close to the single-particle energies obtained in spherical calculations. This shows that deformation polarization effects induced by extra particle or hole are rather modest. In general, they lead to a slight compression of the calculated spectra as compared to those obtained in spherical calculations. Note that the magnitude and impact of deformation polarization effects are similar in our calculations and in the calculations of Ref. [13].

The inclusion of time-odd mean fields induces additional binding in odd-mass nuclei (see Ref. [5] for more detail), which is rather modest being around 100–200 keV in the nuclei around ^{56}Ni. This again introduces a slight compression of the calculated spectra (Fig. 2). One should note that additional binding due to TO mean fields in odd-mass nuclei (and a subsequent compression of the spectra) is substantially larger in the calculations of Ref. [13]. For example, it is around 0.5 MeV in the nuclei around ^{208}Pb and reaches 1–1.5 MeV in ^{56}Ni. Note that, for the latter nucleus, additional binding due to TO mean fields is only 0.1–0.2 MeV in our CRMF calculations (see Fig. 2). The reason for this difference is not clear. However, additional bindings due to TO mean fields in

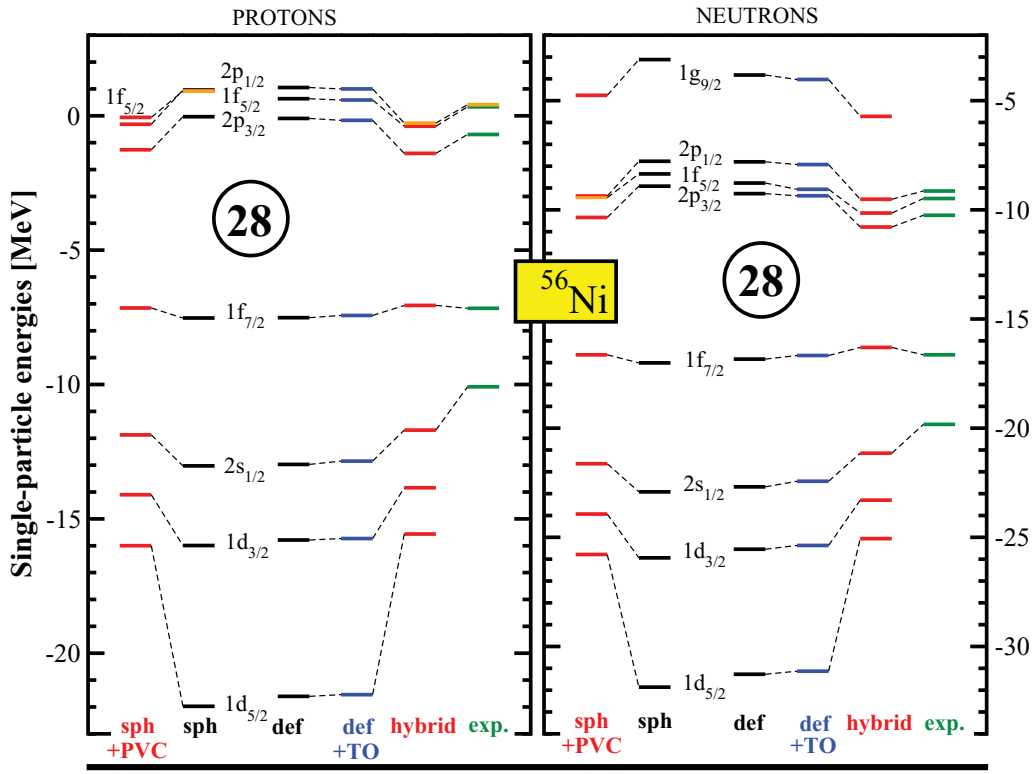

FIG. 2. (Color online) Spectra of ^{56}Ni and its neighboring odd nuclei. Column "sph" shows the single-particle spectra obtained in spherical RMF calculations of ^{56}Ni. Column "sph + PVC" shows the spectra obtained in spherical calculations within the PVC model. Columns "def," "def + TO," "hybrid," and "exp" show one-nucleon separation energies defined according to Eqs. (1) and (2). Column "def" is based on the results of triaxial CRMF calculations with no TO mean fields. These fields are included in the calculations the results of which are shown in column "def + TO". The corrections due to PVC are added in column "hybrid." The experimental single-particle energies are displayed in column "exp;" they are based on the data of Refs. [77] (masses of ground states), [78] (^{55}Ni), [69] (^{55}Co), [30,70] (^{57}Ni), and [30] (^{57}Cu). In order to distinguish overlapping levels, orange and then maroon colors are used for the levels in addition to their standard color used in a given column. See text for more details.

the nuclei under study obtained in our CRMF calculations are within the typical ranges obtained in the systematic study of the impact of TO mean fields on the binding energies of odd mass nuclei (Ref. [5]). In addition, the CRMF code employed here has been extensively and successfully used in the description of rotating systems in which TO fields have very large impact on the moments of inertia (see Refs. [3,41] and references quoted therein). These two facts strongly suggest that the impact of TO mean fields is correctly described in the current work.

The dominant levels (i.e., the levels with the largest spectroscopic factors) as obtained in spherical PVC calculations are shown in column ''sph + PVC". One can see two effects of particle-vibration coupling: (i) the general compression of the spectra leading to a better agreement with experiment and (ii) in some cases the change of the level sequences. With few exceptions, the spectroscopic factors of the dominant levels in the vicinity of the Fermi level vary between 0.5 and 0.9 (see Tables III and IV below), thus these states retain basically their single-particle nature.

The impact of particle-vibration coupling on specific states can be quantified by the energy difference between the energies of this state in the columns "sph" and ''sph + PVC" of Fig. 5. These energy differences, treated as the corrections due to PVC, are then added to one-neutron separation energies obtained in triaxial CRMF calculations; this leads to column "hybrid." The results in this column are compared with experimental data presented in column "exp."

The single-particle spectra of doubly magic ^{100}Sn, ^{132}Sn, and ^{208}Pb nuclei, obtained in the same way as for Fig. 2, are displayed in Figs. 3–5. They show similar effects due to PVC and the polarizations induced by deformation and TO mean fields as in the case of ^{56}Ni. Their details will be discussed below.

Let consider major conclusions emerging from these calculations. They are related to the role of polarizations effects due to deformation and TO mean fields and the impact of PVC on the accuracy of the description of single-particle spectra, shell gaps, pseudospin doublets, and spin-orbit splittings.

B. Polarization effects due to deformation and time-odd mean fields

Combined polarization effects due to deformation and TO mean fields are shown in Fig. 6. Two features are clearly seen.

First, combined polarization effects due to deformation and time-odd mean fields decrease with an increase of mass number. Indeed, with an increase of the size of nucleus the

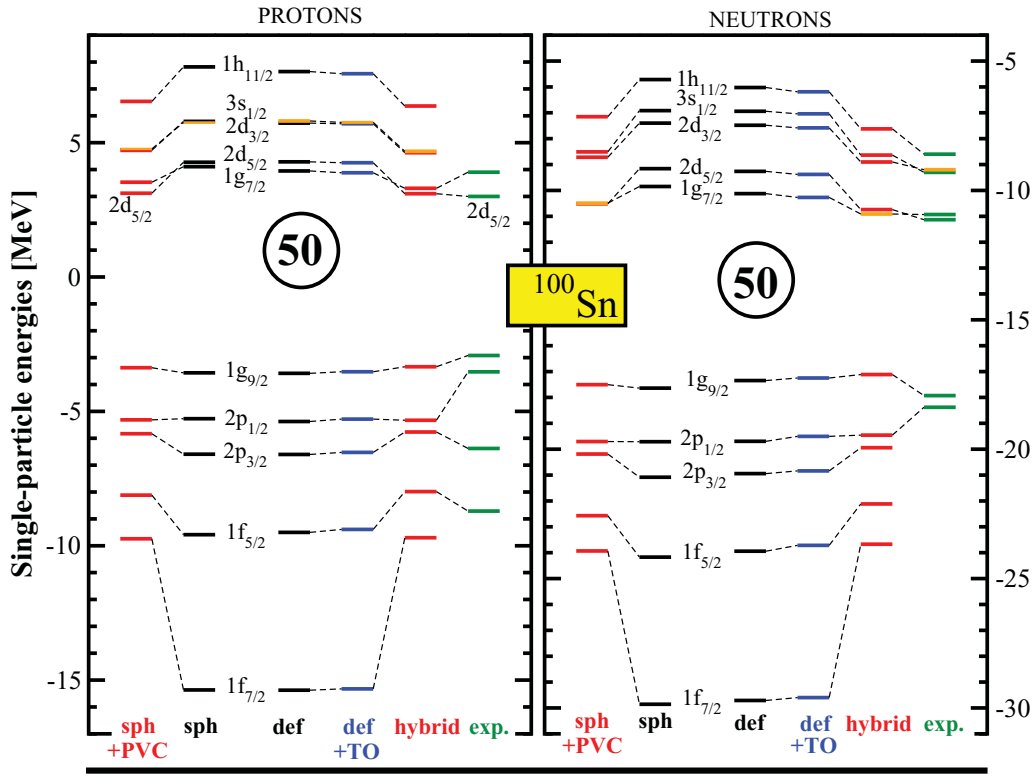

FIG. 3. (Color online) The same as in Fig. 2 but for the spectra of ^{100}Sn. Extrapolated "experimental" single-particle energies of proton and neutron spherical subshells are taken from Ref. [55].

relative role of each single-particle orbital becomes smaller, which leads to the fact that the calculated quadrupole deformations of odd-mass nuclei decrease with an increase of mass. For example, the average proton and neutron deformations of calculated single-particle states in ^{57}Cu and ^{57}Ni are 0.045 and 0.060, respectively. On the contrary, these deformations are significantly smaller in ^{209}Bi and ^{209}Sn; they are only 0.0055 and 0.006, respectively. Thus, odd nuclei neighboring ^{208}Pb remain basically spherical. The decrease of calculated deformations of odd-mass nuclei neighboring doubly magic nuclei with increasing mass clearly indicates that deformation polarization effects also decrease with mass number. In addition, additional binding due to TO mean fields decreases with mass (see Ref. [5] for details). The combination of these two effects is responsible for the features seen in Fig. 6.

Figure 6 also reveals that combined polarization effects due to deformation and TO mean fields are smaller for protons than for neutrons by a factor of approximately two. This is especially true for the $N = Z$ ^{56}Ni and ^{100}Sn nuclei which have the same proton and neutron single-particle states. The part of this difference comes from the fact that additional binding due to TO mean fields is smaller for odd-proton nuclei as compared with odd-neutron nuclei (see Ref. [5]). The analysis of Ref. [5] clearly indicates that the contributions of the Coulomb force to the proton single-particle energies in the presence of TO mean fields are responsible for this feature. Deformation polarization effects show the same features; namely, they are smaller for odd-proton nuclei as compared with odd-neutron nuclei. For example, average deformation polarizations per single-particle state are 0.157 MeV and 0.326 MeV for proton and neutron single-particle states of ^{56}Ni, respectively, and 0.060 MeV and 0.164 MeV for proton and neutron single-particle states of ^{100}Sn, respectively. Similar to the case of polarizations due to TO mean fields, the origin of this difference has to be traced back to the Coulomb force since compared sets of proton and neutron single-particle states are the same in a given $N = Z$ nucleus.

The majority of the comparisons of the energies of the single-particle states obtained in different particle vibration coupling models with experiment neglect deformation and TO mean-field polarization effects induced by the odd particle (see, for example, Refs. [16,17,52]). The current analysis indicates that within the framework of CDFT this neglect is more or less justified only for heavy nuclei, and it is more justified for a proton subsystem than for a neutron subsystem.

C. Accuracy of description of single-particle spectra

The analysis of Figs. 2, 4, and 5 reveals that the inclusion of particle vibration coupling substantially improves the accuracy of the description of single-particle spectra. This statement is quantified in Fig. 7 and Table I.

Figure 7 displays the distribution of the deviations between calculated and experimental energies of the single-particle states in proton and neutron subsystems of ^{56}Ni, ^{132}Sn, and ^{209}Pb. It clearly shows that, on average, the inclusion of particle-vibration coupling substantially improves the description of single-particle spectra, and that neutron single-particle

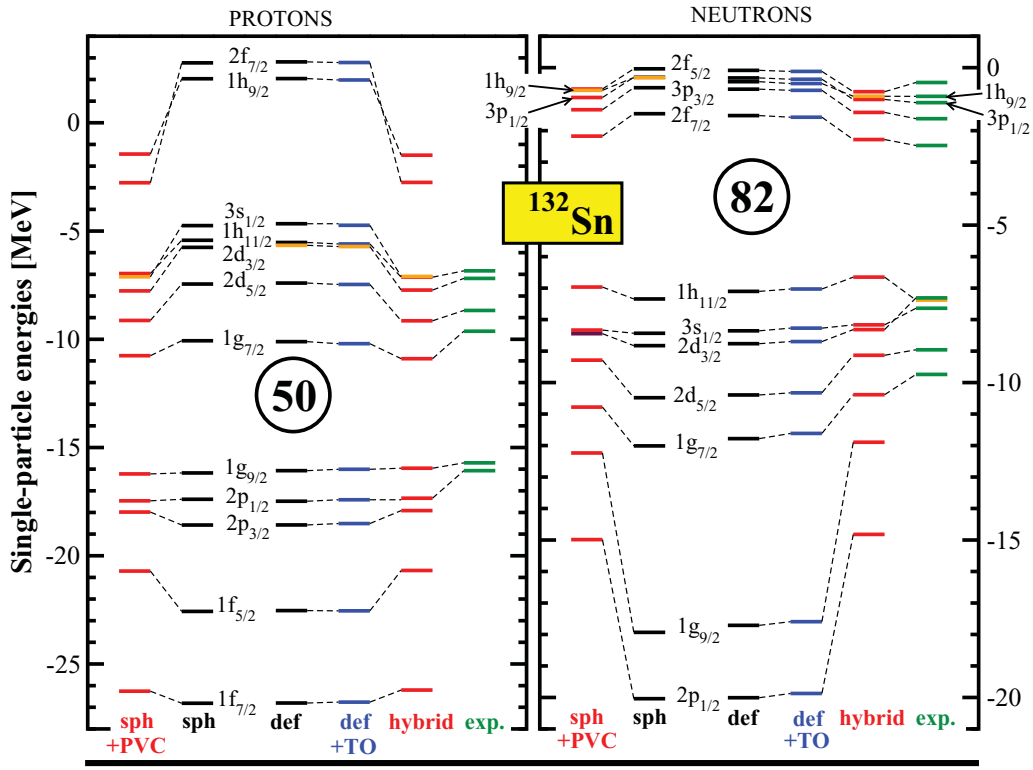

FIG. 4. (Color online) The same as in Fig. 2 but for the spectra of ^{132}Sn. The experimental single-particle energies are based on the data of Refs. [77] (masses of ground states), [71] (^{131}Sn), [72] (^{131}In), [73,74] (^{133}Sb), and [63] (^{133}Sn).

states are better described than their proton counterparts. However, even in the "hybrid" calculations there are few (mostly proton) states which deviate from experiment by more than 1 MeV. Note that the inclusion of particle-vibration coupling can make the agreement between theory and experiment worse for some states. This is seen, for example, in the case of proton $3s_{1/2}$ and $1h_{9/2}$ subshells in ^{208}Pb (Fig. 5).

Average deviations per state, $\Delta\varepsilon$, between calculated and experimental energies of the single-particle states are shown in Table I. They are defined as

$$\Delta\varepsilon = \frac{\sum_{i=1}^{N} \left|\varepsilon_i^{\text{theor}} - \varepsilon_i^{\text{expt}}\right|}{N}, \tag{5}$$

where N is the number of the states with known experimental single-particle energies, and $\varepsilon_i^{\text{theor}}$ ($\varepsilon_i^{\text{expt}}$) are calculated (experimental) energies of the single-particle states. One can see that the inclusion of PVC substantially improves the description of the single-particle states in ^{132}Sn and ^{208}Pb. On the contrary, PVC introduces no (small) improvement in the description of the proton (neutron) single-particle states of ^{56}Ni. It is interesting to mention that the best agreement with experiment is obtained in the "hybrid" calculations of neutron-rich ^{132}Sn.

While the accuracy of the description of proton and neutron states is comparable in ^{56}Ni, neutron states are appreciable better described than proton ones in the "hybrid" calculations of ^{132}Sn and ^{208}Pb. The analysis of Figs. 4 and 5 strongly suggests that the increases of the depth of proton potential in these two nuclei by few hundreds keV (and as a result the lowering of the energies of proton single-particle states by similar energy) will improve the agreement with experiment. This clearly indicates that the inclusion of the single-particle energies into the fit of the CDFT parametrizations can provide extra information on the depth of the proton and neutron potentials and their evolution with particle numbers.

The detailed comparison between theory and experiment has not been performed for ^{100}Sn since very little experimental information is available on neighbouring to ^{100}Sn nuclei with one nucleon less (more) (see, for example, Refs. [53,54]). Unfortunately, the extrapolations of the single-particle energies from other odd nuclei toward ^{100}Sn do not give unique values. This is illustrated in Table II where the results of the extrapolations of Refs. [55,56] are shown. Note that the estimates of the energies of the single-particle states of Ref. [56] coincide within the estimation errors (given in Table II in parentheses) with the values reported in Ref. [55], except for the energy of the $1g_{7/2}$ proton state. However, estimation errors are significant, which makes detailed comparison between theory and experiment meaningless. On the other hand, one can clearly see in Fig. 3 that PVC improves the agreement with experimental estimates.

D. Impact of particle-vibration coupling on shell gaps

The size of the shell gap (between the last occupied and first unoccupied states in even-even doubly magic nuclei) is defined as

$$\delta(Z, N) = \min\{(\varepsilon_i)^{\text{above}}\} - \max\{(\varepsilon_i)^{\text{below}}\}, \tag{6}$$

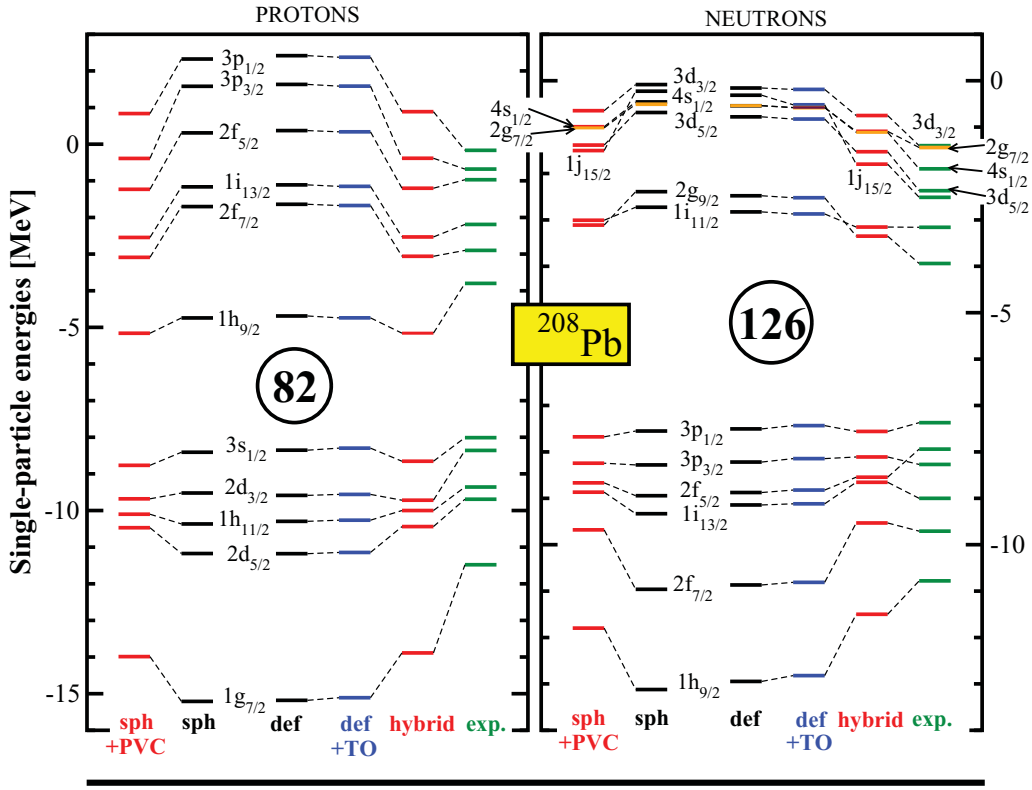

FIG. 5. (Color online) The same as in Fig. 2 but for the spectra of ^{208}Pb. The experimental single-particle levels are based on the data of Refs. [75–77].

where $(\varepsilon_i)^{\text{above}}$ and $(\varepsilon_i)^{\text{below}}$ stand for the energies of the single-particle states above and below the shell gap. This definition of the shell gap incorporates the information from three different nuclei because the single-particle energies are defined according to Eqs. (1) and (2). The advantage of this definition is that it allows to incorporate the polarization (due to deformation and TO mean fields) and PVC effects on the size of the shell gap.

Figure 8 compares experimental shell gaps with the shell gaps obtained in the ''def + TO" and "hybrid" calculations. The extrapolations of Refs. [55,56] for the single-particle energies in ^{100}Sn lead to quite different values of the proton $Z = 50$ shell gap. It is reasonable to expect the same situation for the neutron $N = 50$ shell gap, the size of which, however, cannot be determined in the extrapolations of Ref. [56] since no estimates for the single-particle states below it are provided (see Table II).

The shell gaps are largest in the spherical mean-field calculations. The gaps become smaller with the inclusion of each additional type of correlations. The inclusion of polarization effects due to deformation and TO mean fields decreases slightly their sizes (see Figs. 2–5). Thus, we compare with experiment in Fig. 8 only the PVC ("hybrid") and best mean-field ("def + TO") calculations. This figure shows that particle-vibration coupling decreases substantially the size of the shell gaps. The effect is most pronounced in ^{56}Ni where PVC decreases the proton $Z = 28$ and neutron $N = 28$ shell gaps by almost 2 MeV. On the contrary, the effect of particle-vibration coupling is least pronounced in ^{208}Pb in which it decreases the size of the neutron $N = 126$ gap by only few hundred keV and has almost no impact on the proton $Z = 82$ shell gap.

Comparing experimental and calculated shell gaps in ^{56}Ni, ^{132}Sn, and ^{208}Pb, one can conclude that both calculational schemes provide similar accuracy of the description of experimental data. However, experimental shell gaps are typically overestimated in the "def + TO" calculations. The exceptions are the $Z = 50$ gap in ^{132}Sn and the $Z = 82$ gap in ^{208}Pb. On the contrary, with the exception of the $N = 126$ gap in ^{208}Pb, the size of the experimental gaps is underestimated in the calculations with particle-vibration coupling.

E. Spectroscopic factors

The calculated spectroscopic factors for odd nuclei with doubly-magic cores are compared with experiment in Tables III and IV. In odd nuclei neighboring ^{208}Pb, the experimental spectroscopic factors are reasonably well reproduced in the PVC calculations. Both in experiment and in calculations the proton states are found to be somewhat more fragmented than the neutron states. When comparing theory with experiment one should keep in mind that the experimental spectroscopic factors depend considerably on the parameters used in the model analysis and on the reaction employed, which is clearly seen in the staggering of experimental values. Note that the results obtained for ^{208}Pb with the NL3* parametrization are very close to those obtained previously in Ref. [17] with the NL3 force.

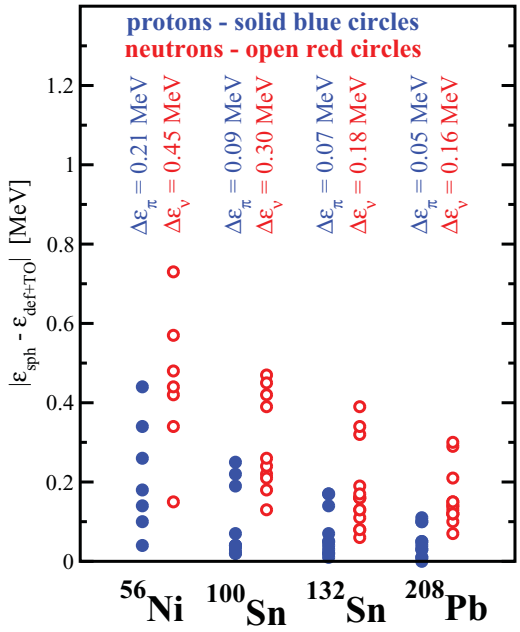

FIG. 6. (Color online) Combined polarization effects due to deformation and time-odd mean fields. For each single-particle state of Figs. 2–5, the absolute values of the difference of the energies obtained in spherical (the $\varepsilon_{\rm sph}$ energies; column "sph" in Figs. 2–5) and deformed (the $\varepsilon_{\rm def+TO}$ energies of the calculations with TO mean fields included; column "def + TO" in Figs. 2–5) calculations are shown. The average polarization effects per state $\Delta\varepsilon_k$ ($k = \pi, \nu$) are also shown.

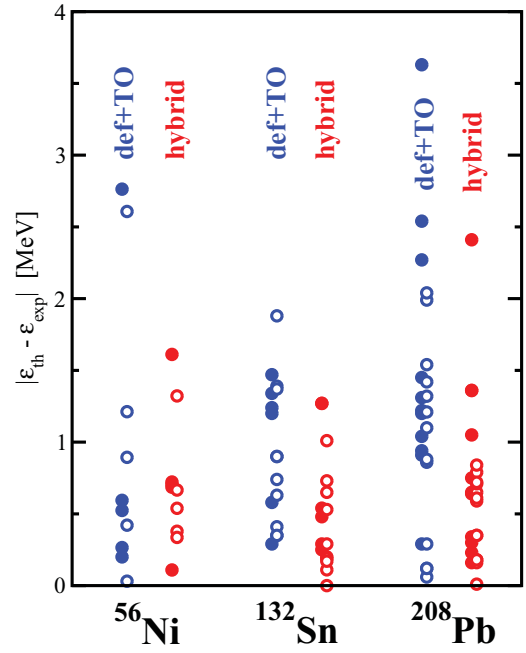

FIG. 7. (Color online) The deviations of calculated energies of the single-particle states from experimental states obtained in the "def + TO" and "hybrid" calculational schemes for indicated nuclei. The results for proton and neutron states are given by solid and open circles.

For other nuclei, the experimental data are available only for ^{133}Sn (Table III) and ^{57}Ni (Table IV). The level of agreement between theory and experiment in ^{133}Sn is comparable with that seen in odd nuclei neighboring ^{208}Pb. The situation in ^{57}Ni is more controversial. For example, the sum rule (3) is strongly violated in the case of the $1f_{5/2}$ state in the experimental data of Ref. [64]. In addition, experimental spectroscopic factors for the $2p_{3/2}$ state in ^{57}Ni extracted by means of the (d, p) transfer [34] and one-neutron knockout [64] reactions differ by a factor of almost two. Currently, there is no satisfactory explanation for this difference (Ref. [34]). The results of the PVC calculations are lower than the experimental values obtained in the (d, p) transfer reaction but higher than the ones obtained in the one-neutron knockout reaction. On the other hand, the spectroscopic factors obtained in the PVC calculations are very close to the ones obtained in the spherical shell model calculations in full fp model space which employ the GXPF1A interaction (see Table II in Ref. [34]). Note that the latter calculations provide the best agreement with the data for Ni isotopes [34]. One should also mention that nonrelativistic particle-vibration calculations of Ref. [65] give the spectroscopic factors for the $2p_{3/2}$, $1f_{5/2}$, and $2p_{1/2}$ states which are very close to 0.6.

F. Impact of particle-vibrational coupling on spin-orbit splittings

Covariant density functional theory naturally describes the spin-orbit interaction in nuclei [1,2], which is a relativistic effect that has to be added phenomenologically in nonrelativistic models. The comparison of experimental spin-orbit splittings with calculations has been performed only at the mean-field level so far (see, for example, Refs. [4,13]). However, the current work clearly indicates that particle-vibration coupling has an impact on the energies of the single-particle states. Thus, it is reasonable to expect that it will also modify the spin-orbit splittings.

TABLE II. Extrapolated "experimental" single-particle energies of spherical proton and neutron subshells in ^{100}Sn. The results of the extrapolations of Refs. [55,56] are shown.

Subshell	ε_i [MeV] [55]	ε_i [MeV] [56]
	Neutrons	
$1h_{11/2}$	−8.6(5)	−7.8(8)
$2d_{3/2}$	−9.2(5)	−8.8(8)
$3s_{1/2}$	−9.3(5)	−9.3(9)
$2g_{7/2}$	−10.93(20)	−10.4(10)
$2d_{5/2}$	−11.13(20)	−11.1(10)
$1g_{9/2}$	−17.93(30)	
$2p_{1/2}$	−18.38(20)	
	Protons	
$1g_{7/2}$	+3.90(15)	2.6(3)
$2d_{5/2}$	+3.00(80)	2.8(3)
$1g_{9/2}$	−2.92(20)	−2.9(3)
$2p_{1/2}$	−3.53(20)	−3.5(3)
$2p_{3/2}$	−6.38	
$1f_{5/2}$	−8.71	

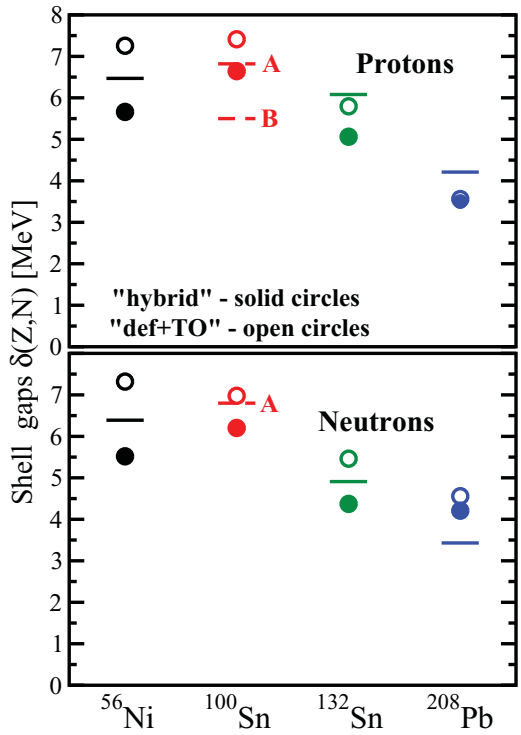

FIG. 8. (Color online) The size of proton and neutron shell gaps. The results of the "def + TO" and "hybrid" calculations are compared with experimental values shown by horizontal lines. In the case of ^{100}Sn, the experimental shell gaps are extracted from extrapolated single-particle energies of Refs. [55] (A) and [56] (B) [see also Table II]. Note that the size of the $Z = 82$ shell gap in ^{208}Pb is almost the same in both calculations.

In order to understand the impact of polarization effects (due to deformation and TO mean fields) and particle-vibration coupling on spin-orbit splittings, the results of the "sph," "sph + PVC," "def," "def + TO," and "hybrid" calculations are compared with available experimental data on the spin-orbit doublets in Figs. 9–11.

The impact of deformation and TO mean-field polarization effects on spin-orbit splittings is rather modest in ^{208}Pb (Fig. 9) since these effects are smallest in heavy systems (see Sec. IV B). In addition, both of them lead to a compression of the single-particle spectra. As a consequence, they act in the same direction for the members of the spin-orbit doublet, which is built either from hole (below the shell gap) or particle (above the shell gap) states. Moreover, these polarization effects are more or less similar in magnitude for the members of such spin-orbit doublets. As a consequence, they cancel to a large extent when spin-orbit splitting is calculated as the difference of the energies of the members of the spin-orbit doublet. Such behavior is typical for the spin-orbit doublets based on the orbitals with low orbital angular momentum l, both members of which are located either below or above the shell gap. For this type of the spin-orbit doublets, the impact of polarization effects on spin-orbit splittings is also small in ^{132}Sn (Fig. 10). However, it becomes more pronounced (especially in the neutron subsystem) in ^{56}Ni (Fig. 11).

The situation is different for the spin-orbit doublets built on the orbitals with high orbital angular momentum l. For such doublets, one member is located above the shell gap, while another below the shell gap. The compression of the single-particle spectra due to deformation and TO mean-field polarization effects leads to the decrease of spin-orbit splitting. This decrease is especially pronounced for light nuclei and for the neutron subsystem in a given nucleus (compare Figs. 11, 10, and 9) because of particle number and subsystem (proton or neutron) dependencies of the polarization effects discussed in Sec. IV B.

The impact of particle-vibration coupling on spin-orbit splittings is state-dependent. It is small or modest in the proton $l = 3(2f_{7/2}–2f_{5/2})$ and neutron $l = 1$ $(3p_{3/2}–3p_{1/2})$, $l = 2$ $(2d_{5/2}–2d_{3/2})$ and $l = 4$ $(2g_{9/2}–2g_{7/2})$ doublets of ^{208}Pb (Fig. 9), proton $l = 2$ $(2d_{5/2}–2d_{3/2})$ and neutron $l = 1$ $(3p_{3/2}–3p_{1/2})$ and $l = 3$ $(2f_{7/2}–2f_{5/2})$ doublets of ^{132}Sn (Fig. 10), and neutron and proton $l = 1(2p_{3/2}–2p_{1/2})$ doublets in ^{56}Ni (Fig. 11). In these doublets, the corrections to the energies of the members of the spin-orbit doublet due to PVC are more or less the same.

However, this is not always the case for the doublets based on the orbitals with low orbital angular momentum l. For example, the corrections due to PVC differ significantly for the proton $3d_{3/2}$ and $3d_{5/2}$ states of ^{208}Pb (Fig. 5). As a consequence, particle-vibration coupling significantly affects the spin-orbit splitting of the proton $l = 2$ $(3d_{5/2}–3d_{3/2})$ doublet. In addition, spin-orbit splittings of the proton $l = 1$ $(3p_{3/2}–3p_{1/2})$ and neutron $l = 3$ $(2f_{7/2}–2f_{5/2})$ doublets in ^{208}Pb (Fig. 9) as well as of the neutron $l = 2$ $(2d_{5/2}–2d_{3/2})$ doublet in ^{132}Sn (Fig. 10) are strongly affected by particle-vibration coupling.

The effect of particle-vibration coupling is especially pronounced for the spin-orbit doublets with high orbital angular momentum l, the one member of which is located below the shell gap and another above the shell gap. These are the proton $l = 5\,(1h_{11/2}–1h_{9/2})$ and neutron $l = 6\,(1i_{13/2}–1i_{11/2})$ doublets in ^{208}Pb (Fig. 9), the proton $l = 4\,(1g_{9/2}–1g_{7/2})$ and neutron $l = 5\,(1h_{11/2}–1h_{9/2})$ doublets in ^{132}Sn (Fig. 10), and the proton and neutron $l = 3\,(1f_{7/2}–1f_{5/2})$ doublets in ^{56}Ni (Fig. 11). For these doublets, the spin-orbit splittings are largest in spherical calculations. The inclusion of polarization effects due to deformation and TO mean fields decreases these splittings. The PVC coupling further reduces the energy splittings by approximately 1 MeV in medium- and heavy-mass nuclei (Figs. 9 and 10) and by approximately 1.5 MeV in ^{56}Ni (Fig. 11).

It is interesting to compare these results with those obtained in the nonrelativistic PVC model of Ref. [52] based on the Skyrme energy density functional. Such a comparison is possible only for neutron spin-orbit doublets of ^{208}Pb. The impact of PVC on spin-orbit splittings in the nonrelativistic model can be extracted by comparing the columns "tensor included" and "PVC included" of Fig. 6 in Ref. [52] and compare with our results shown in the right panel of Fig. 9 (or the right panel of Fig. 5). It turns out that relativistic and nonrelativistic models show similar changes (both direction [increase or decrease] and magnitude) in spin-orbit splittings induced by PVC in the majority of the cases. In both models, PVC leads to small increase [decrease] by approximately

TABLE III. Spectroscopic factors S of the dominant single-particle levels in odd nuclei surrounding ^{208}Pb and ^{132}Sn calculated within the relativistic particle-vibration coupling model compared to experimental data. The experimental data are taken from Refs. [57] [^{209}Bi, (^{3}He,d) reaction], [36] [^{209}Bi, the (α,t) reaction], [35] [^{207}Tl, the (d,^{3}He) reaction], [58] [^{207}Tl, the (t, α) reaction], [59] [^{207}Pb, the (d,t) reaction], [60] [^{207}Pb, the (^{3}He,α) reaction], [61] [^{209}Pb, the (d, p) reaction], [62] [^{209}Pb, the (α, ^{3}He) reaction], and [63] [^{133}Sn, the (d, p) reaction]. For comparison the experimental data from two different reactions are presented for odd-mass nuclei neighboring ^{208}Pb.

Nucleus	State	S_{theor}	S_{expt}	S_{expt}	Nucleus	State	S_{theor}	S_{expt}
^{209}Pb	$2g_{9/2}$	0.85	0.78 ± 0.1 [61]	0.94 [62]	^{133}Sn	$2f_{7/2}$	0.89	0.86 ± 0.16
	$1i_{11/2}$	0.89	0.96 ± 0.2 [61]	1.05 [62]		$3p_{3/2}$	0.91	0.92 ± 0.18
	$1j_{15/2}$	0.66	0.53 ± 0.2 [61]	0.57 [62]		$1h_{9/2}$	0.88	
	$3d_{5/2}$	0.89	0.88 ± 0.1 [61]			$3p_{1/2}$	0.91	1.1 ± 0.3
	$4s_{1/2}$	0.92	0.88 ± 0.1 [61]			$2f_{5/2}$	0.89	1.1 ± 0.2
	$2g_{7/2}$	0.87	0.78 ± 0.1 [61]					
	$3d_{3/2}$	0.89	0.88 ± 0.1 [61]					
^{209}Bi	$1h_{9/2}$	0.88	1.17 [57]	0.80 [36]	^{133}Sb	$1g_{7/2}$	0.86	
	$2f_{7/2}$	0.78	0.78 [57]	0.76 [36]		$2d_{5/2}$	0.82	
	$1i_{13/2}$	0.63	0.56 [57]	0.74 [36]		$2d_{3/2}$	0.63	
	$2f_{5/2}$	0.61	0.88 [57]	0.57 [36]		$1h_{11/2}$	0.79	
	$3p_{3/2}$	0.62	0.67 [57]	0.44 [36]		$3s_{1/2}$	0.70	
	$3p_{1/2}$	0.37	0.49 [57]	0.20 [36]				
^{207}Pb	$3p_{1/2}$	0.90		1.08 [60]	^{131}Sn	$2d_{3/2}$	0.88	
	$2f_{5/2}$	0.87	1.13 [59]	1.05 [60]		$1h_{11/2}$	0.86	
	$3p_{3/2}$	0.86	1.00 [59]	0.95 [60]		$3s_{1/2}$	0.87	
	$1i_{13/2}$	0.82	1.04 [59]	0.61 [60]		$2d_{5/2}$	0.70	
	$2f_{7/2}$	0.64	0.89 [59]	0.64 [60]		$1g_{7/2}$	0.72	
	$1h_{9/2}$	0.38						
^{207}Tl	$3s_{1/2}$	0.84	0.95 [58]	0.85 [35]	^{131}In	$1g_{9/2}$	0.85	
	$2d_{3/2}$	0.86	1.15 [58]	0.90 [35]		$2p_{3/2}$	0.70	
	$1h_{11/2}$	0.80	0.89 [58]	0.88 [35]		$2p_{1/2}$	0.85	
	$2d_{5/2}$	0.68	0.62 [58]	0.63 [35]		$1f_{5/2}$	0.37	
	$1g_{7/2}$	0.22	0.40 [58]	0.27 [35]				

TABLE IV. Spectroscopic factors S of the dominant single-particle levels in odd nuclei surrounding ^{100}Sn and ^{56}Ni calculated within the relativistic particle-vibration coupling model. They are compared to the experimental values extracted by means of the (d, p) transfer [34] and one-neutron knockout [64] reactions in the case of ^{57}Ni.

Nucleus	State	S_{theor}	Nucleus	State	S_{theor}	S_{expt} [34]	S_{expt} [64]
^{101}Sn	$2d_{5/2}$	0.85	^{57}Ni	$2p_{3/2}$	0.83	0.95 ± 0.29	0.58 ± 0.11
	$1g_{7/2}$	0.85		$1f_{5/2}$	0.79	1.40 ± 0.42	
	$2d_{3/2}$	0.78		$2p_{1/2}$	0.76	1.00 ± 0.30	
	$3s_{1/2}$	0.81		$1g_{9/2}$	0.79		
	$1h_{11/2}$	0.80					
^{101}Sb	$2d_{5/2}$	0.87	^{57}Cu	$2p_{3/2}$	0.85		
	$1g_{7/2}$	0.86		$1f_{5/2}$	0.80		
	$2d_{3/2}$	0.83		$2p_{1/2}$	0.80		
	$3s_{1/2}$	0.87		$1g_{9/2}$	0.80		
	$1h_{11/2}$	0.81					
^{99}Sn	$1g_{9/2}$	0.84	^{55}Ni	$1f_{7/2}$	0.78		
	$2p_{1/2}$	0.85		$2s_{1/2}$	0.71		
	$2p_{3/2}$	0.71		$1d_{3/2}$	0.62		
	$1f_{5/2}$	0.62		$1d_{5/2}$	0.20		
	$1f_{7/2}$	0.11					
^{99}In	$1g_{9/2}$	0.85	^{55}Co	$1f_{7/2}$	0.78		
	$2p_{1/2}$	0.86		$2s_{1/2}$	0.73		
	$2p_{3/2}$	0.73		$1d_{3/2}$	0.64		
	$1f_{5/2}$	0.66		$1d_{5/2}$	0.20		
	$1f_{7/2}$	0.14					

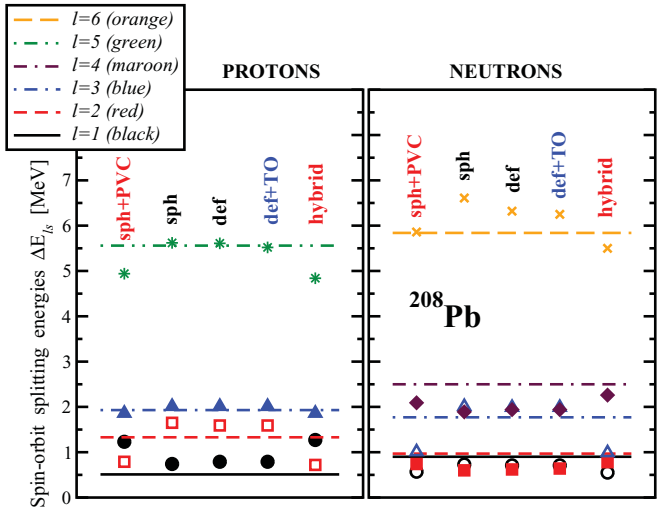

FIG. 9. (Color online) Spin-orbit splitting energies ΔE_{ls} of the spin-orbit doublets in ^{208}Pb. Inset shows the colors used for different values of orbital angular momentum l. Theoretical results are shown by symbols, while the experimental values by solid lines. Solid (open) symbols are used for spin-orbit doublets which are build from the particle (hole) states with respect of the ^{208}Pb core. The stars and crosses are used for the spin-orbit doublets which involve both particle and hole states.

0.15 MeV of the splitting of the $l = 2$ $(3d_{5/2}–3d_{3/2})$ $[l = 1$ $(3p_{3/2}–3p_{1/2})]$ spin-orbit doublet. The spin-orbit splittings of the $l = 3$ $(2f_{7/2}–2f_{5/2})$ (located below the $N = 126$ shell gap) and $l = 6$ $(1i_{13/2}–1i_{11/2})$ (the members of the doublet located below and above the $N = 126$ shell gap) doublets are decreased by approximately 0.5 MeV in the nonrelativistic model and by approximately 0.9 MeV in the relativistic model when PVC is taken into account. The difference exists only in the case of the $l = 4$ $(2g_{9/2}–2g_{7/2})$ spin-orbit doublet, the splitting of which is slightly decreased by PVC in nonrelativistic calculations and increased by 0.3 MeV in relativistic calculations.

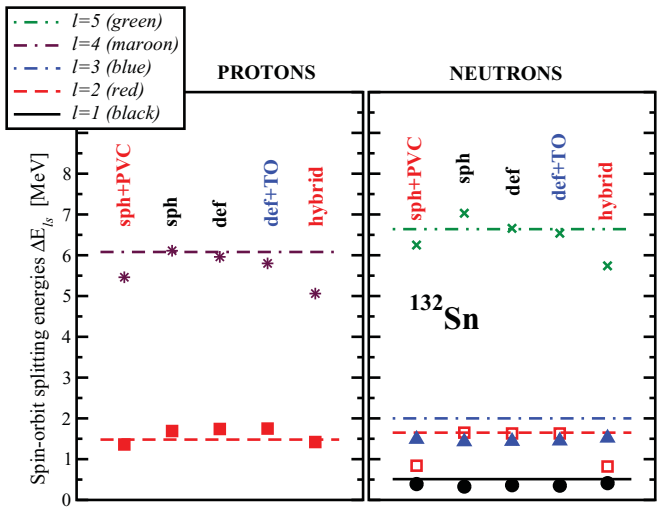

FIG. 10. (Color online) The same as in Fig. 9 but for the spin-orbit doublets of ^{132}Sn.

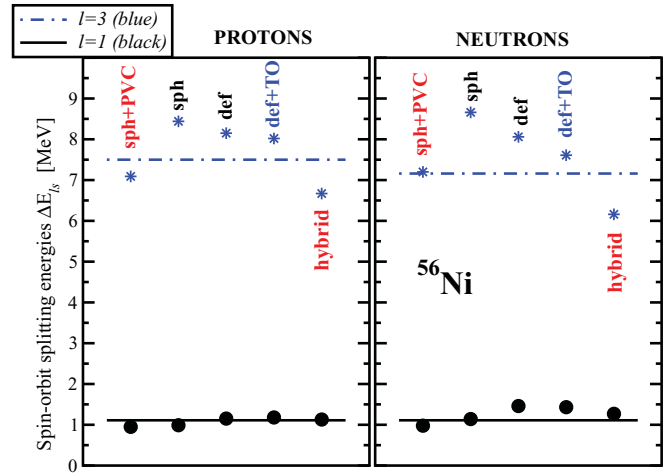

FIG. 11. (Color online) The same as in Fig. 9 but for the spin-orbit doublets of ^{56}Ni.

Fig. 12 presents percent deviations $\delta(\Delta E_{ls})$ of the calculated spin-orbit splittings from experimental splittings defined as

$$\delta(\Delta E_{ls}) = \frac{\Delta E_{ls}^{\text{theor}} - \Delta E_{ls}^{\text{expt}}}{\Delta E_{ls}^{\text{expt}}} \times 100\%, \qquad (7)$$

where ΔE_{ls} is the spin-orbit splitting energy. Negative (positive) values of $\delta(\Delta E_{ls})$ indicate that experimental spin-orbit splitting is underestimated (overestimated) in the calculations. One can see that, on average, the mean-field results are more or less evenly scattered around zero percent deviation. On the contrary, with few exceptions, particle-vibration coupling calculations underestimate experimental spin-orbit splittings. Spin-orbit doublets built on the orbitals with high orbital momentum l, involving the members across the shell gap, are rather well (within the 20% deviation) described in both calculations. These doublets are characterized by large spin-orbit splittings ΔE_{ls} in the range of 5–7 MeV, so the 20% deviation means that the absolute deviation from experiment is typically less than 1 MeV. The largest percent deviations are observed for the spin-orbit doublets built on the orbitals with low orbital angular momentum l. These doublets are characterized by low spin-orbit splittings so relatively low absolute deviations from experimental values of the order of a few hundred keV result in appreciable percent deviations.

The analysis of the results of calculations allows us to conclude that the inclusion of particle-vibration coupling decreases the accuracy of the description of spin-orbit splittings. This is clearly visible when absolute and/or percent deviations per doublet are compared in the mean-field and PVC calculations. The absolute deviations per doublet are 0.34 MeV (0.50 MeV), 0.23 MeV (0.56 MeV), and 0.26 MeV (0.45 MeV) in the mean-field ("def + TO") [particle-vibration coupling ("hybrid")] calculations in ^{56}Ni, ^{132}Sn, and ^{208}Pb, respectively. The percent deviations per doublet are 11.8 % (10.3%), 14% (21.5%), and 19.3% (36.4%) in the mean field ("def + TO") [particle-vibration coupling ("hybrid")] calculations in ^{56}Ni, ^{132}Sn, and ^{208}Pb, respectively.

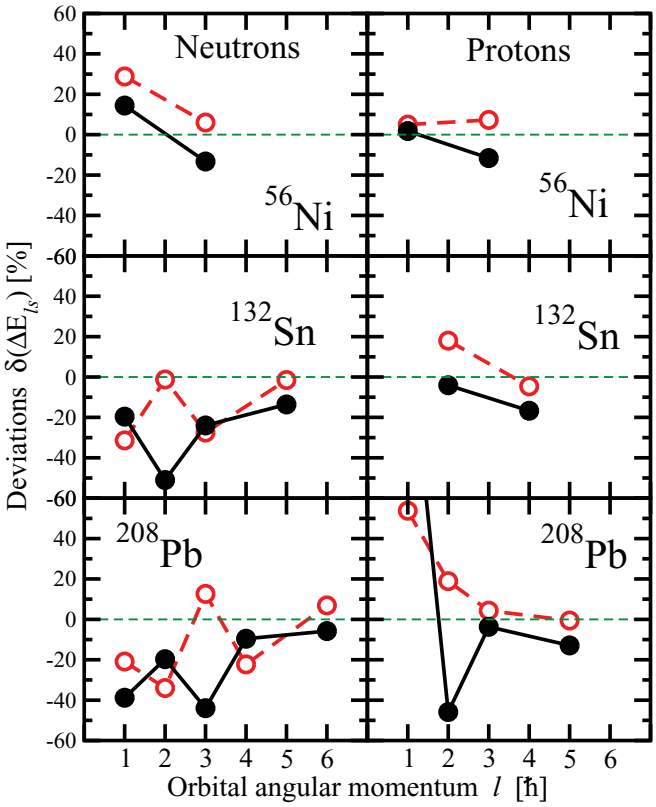

FIG. 12. (Color online) Percent deviations of the spin-orbit splittings in the "def + TO" (red open circles connected by dashed lines) and "hybrid" (black solid circles connected by solid lines) from the experimental values.

These results are not surprising and should not be viewed negatively. First of all, as discussed in Secs. II and IV E, the experimental levels are not pure single-particle levels, and as such they are closer in nature to the calculated levels of the PVC model. Second, relativistic description [1] predicts a definite connection between the Dirac effective mass m^*_D/m of the nucleon in the kinetic energy and the strength of the spin-orbit force because the same effective mass appears in both terms. In addition, the spin-orbit term is sensitive to the spatial variations of the effective mass. Particle-vibration coupling affects the effective mass of the nucleon and as a result it has an impact on calculated spin-orbit splittings. Third, these results point to a new direction of improving the covariant energy density functionals. This is because empirical energy spacings between spin-orbit partner states in finite nuclei determine a relatively narrow interval of allowed values for the Dirac effective mass $0.57 \leqslant m^*_D/m \leqslant 0.61$ on the mean-field level [25]. The observed impact of particle-vibration coupling on spin-orbit splittings suggests that this interval of the Dirac effective mass m^*_D/m may in reality be broader.

G. Impact of particle-vibrational coupling on pseudospin doublets

It was shown in Ref. [6] that quasidegenerate pseudospin doublets in nuclei, discovered more than 40 years ago [66,67], arise from the near equality in magnitude of attractive scalar S and repulsive vector V relativistic mean fields in which the nucleons move.[3] Pseudospin doublets have nonrelativistic quantum numbers $(n_r, l, j = l + 1/2)$ and $(n_r - 1, l + 2, j = l + 1/2)$ where n_r, l, and j are the single-nucleon radial, orbital, and total angular momentum quantum numbers, respectively.[4]

The pseudospin doublet can be characterized by pseudospin doublet splitting energy which is defined as the difference of the energies of pseudospin doublet members

$$\Delta E = E_{n_r,l,j=l+1/2} - E_{(n_r-1),(l+2),j=l+3/2}. \quad (8)$$

With this definition of ΔE, the low-l (high-l) member of the pseudospin doublet is higher in energy than its high-l (low-l) counterpart if $\Delta E > 0$ ($\Delta E < 0$). Note that the calculations fail to reproduce the relative order (in energy) of the members of pseudospin doublet if the signs of ΔE are different in the calculations and experiment.

Figure 13 compares available experimental data on pseudospin-doublet splitting energies in ^{56}Ni, ^{132}Sn, and ^{208}Pb with PVC ("hybrid") and best mean-field ("def + TO") calculations. Note that the ΔE values obtained in the "sph" and "def" calculations deviate from the ones obtained in the "def + TO" calculations by less than 200 keV (in the majority of cases the difference is less than 100 keV). This is because both members of the pseudospin doublet are located either above or below the shell gaps. The polarization effects due to deformation and TO mean fields act in the same direction for these states. As a result, these effects cancel each other to a large degree when the difference of the energies of the members of pseudospin doublet is taken.

Figure 13 clearly shows that particle-vibration coupling substantially improves the description of splitting energies in pseudospin doublets; the average deviations from experiment for ΔE are 0.93 MeV and 0.6 MeV in the mean-field and PVC calculations, respectively. There are still some doublets in which the energy splitting ΔE is poorly reproduced in model calculations. These are the $\pi 2d_{5/2}1g_{7/2}$, and $\pi 2f_{7/2}1h_{9/2}$ doublets in ^{208}Pb (see Figs. 5 and 13), the ΔE values of which deviate from experiment by 2.18 MeV (1.66 MeV) and 2.16 MeV (1.2 MeV) in the mean-field (PVC) calculations, respectively. We did not find clear explanation for such large differences.

Proton and neutron pseudospin doublets with the same single-particle structure have similar splitting energies in experiment (see pseudospin doublets indicated by the brackets with arrows in Fig. 13). This feature is rather well reproduced both in the mean-field and PVC calculations for the proton and neutron $2p_{3/2}1f_{5/2}$ pseudospin doublets of ^{56}Ni. On the contrary, the mean-field ("def + TO") calculations completely fail to reproduce this feature for the proton and neutron $2d_{5/2}1g_{7/2}$ pseudospin doublets in ^{132}Sn and $2f_{7/2}1h_{9/2}$

[3] An extensive review of the manifestations of pseudospin symmetry in different physical systems is presented in Ref. [68].

[4] Note that, in the current paper, the single-particle subshells are labeled by the labels which use $(n_r + 1)$ in the first position of the label.

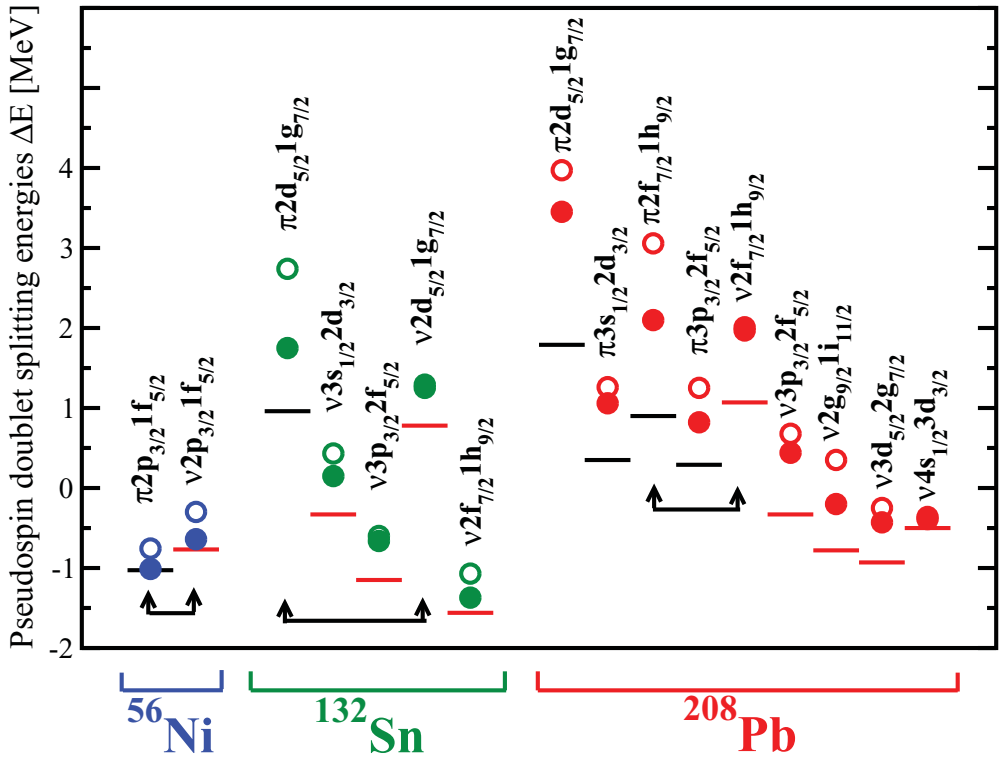

FIG. 13. (Color online) Pseudospin doublet splitting energies in ^{56}Ni, ^{132}Sn, and ^{208}Pb. Experimental data are shown by horizontal lines; black lines are for protons, red for neutrons. The results of the "def + TO" and "hybrid" calculations are shown by open and solid circles, respectively. If both results are close in energy only the solid circle is visible. Brackets with arrows indicate proton and neutron pseudospin doublets with the same single-particle structure. The doublets are labeled by the spherical subshell labels of their members.

pseudospin doublets in ^{208}Pb (Fig. 13); the calculated splitting energies for neutron doublets are more than 1 MeV larger than the ones for proton doublets. However, in the PVC calculations the splitting energies for these pairs of proton and neutron pseudospin doublets are similar in agreement with experiment. This is a consequence of the fact that particle-vibration coupling decreases (as compared with mean-field calculations) the splitting energies in neutron pseudospin doublets by more than 1 MeV leaving at the same time the splitting energies in proton pseudospin doublets unchanged.

H. $^{292}_{172}$120 nucleus: Center of island of stability for superheavy nuclei

The superheavy ^{292}120 nucleus has been predicted to have proton $Z = 120$ and neutron $N = 172$ spherical shell closures within the RMF theory [4]. Thus, it represents the center of the "island of stability" of shell-stabilized superheavy nuclei. The analysis of the deformed one-quasiparticle states in the $A \sim 250$ mass regions in Ref. [22] supports the presence of the $Z = 120$ shell gap in superheavy nuclei. In addition, it indicates $N = 172$ as a likely candidate for magic neutron number in superheavy nuclei.

This nucleus represents a challenge for future experimental synthesis since it is located at the limits of accessibility by available cold fusion reactions. Therefore, as accurate as possible estimations of its characteristics are needed from the theoretical side. First results for its single-particle spectra obtained within the relativistic particle-vibration coupling model are presented in Fig. 14. They are compared with the results obtained on the mean-field level. Note that we restrict ourselves in the case of the ^{292}120 nucleus to spherical calculations. This is because the polarization effects due to deformation and TO mean fields decrease with mass (see Sec. IV B), and thus their impact on the single-particle spectra is expected to be rather small in the ^{292}120 nucleus.

The density of the single-particle states is substantially larger than in lighter nuclei at the mean-field level. As a consequence, this nucleus exhibits a very rich spectrum of low-lying collective phonons already within the RRPA. For example, the lowest vibrational 2^+_1 mode appears at 1.41 MeV with $B(E2)\uparrow = 7.1 \times 10^3 e^2$ fm^4, accompanied by several rather collective modes at 3.18 MeV, 5.25 MeV, 6.74 MeV, etc. A similar picture is obtained for other multipolarities. Although contributions to the nucleonic self-energy from the high-lying modes decrease quickly with energy, we have included phonons with all J^π values mentioned in Sec. III D below 15 MeV (altogether about 100 phonons).

Figure 14 shows that the particle-vibration coupling gives rise to the general compression of the spectra. As a consequence, the size of the $Z = 120$ shell gap decreases from 3.35 MeV (in mean field calculations) down to 2.67 MeV (in the PVC calculations), and the size of the neutron shell gap at $N = 172$ from 2.42 MeV down to 1.83 MeV. Although these gaps are smaller by 20%–25% than the ones obtained

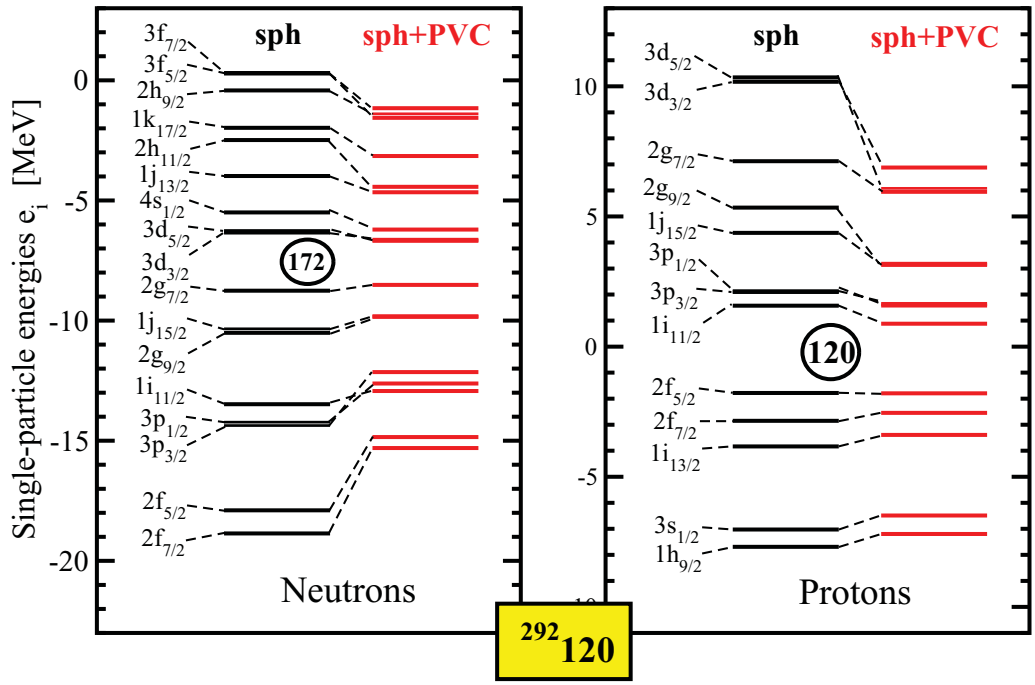

FIG. 14. (Color online) Single-particle spectra of the $^{292}120$ nucleus. Column "sph" shows the single-particle spectra obtained in spherical RMF calculations. Column "sph + PVC" shows the spectra obtained in spherical calculations within the PVC model.

in the mean-field calculations, they are still significant. As a result, the $^{292}120$ nucleus still remains a doubly magic nucleus representing the center of the "island of stability" of superheavy nuclei even when the correlations beyond mean field are taken into account.

V. CONCLUSIONS

The relativistic particle-vibration model has been systematically applied in combination with the cranked relativistic mean-field approach for the study of the impact of surface vibrations on single-particle motion. The polarization effects in odd-mass nuclei due to deformation and time-odd mean fields have been treated in the CRMF framework. The main results can be summarized as follows:

(i) Particle-vibration coupling has to be taken into account when model calculations are compared with experiment since this coupling is responsible for observed fragmentation of experimental levels. The inclusion of particle-vibration coupling substantially improves the description of the energies of dominant single-particle states in ^{132}Sn and ^{208}Pb. However, the accuracy of the description of single-particle spectra in ^{56}Ni is similar in the mean-field and PVC calculations. Note that dominant neutron single-particle states are, on average, better described than proton states in the PVC calculations.

(ii) The polarization effects in odd-mass nuclei due to deformation and time-odd mean fields induced by odd particles are important. They have to be taken into account when experimental and calculated single-particle energies are compared. However, they are usually neglected when the results of particle-vibration coupling model calculations are compared with experiment. The current analysis indicates that, within the framework of CDFT, this neglect is more or less justified only for heavy nuclei, and it is more justified for proton subsystems than for neutron subsystems.

(iii) Particle-vibration coupling leads to a shrinkage of the shell gaps. The size of the shell gaps is typically underestimated in the PVC calculations as compared with experiment and overestimated in the mean-field calculations.

(iv) The inclusion of particle-vibration coupling decreases the accuracy of the description of spin-orbit splittings. The analysis suggests that the mean-field constraint on the allowed range of the Dirac effective mass $0.57 \leqslant m^*_D/m \leqslant 0.61$ is too restrictive and the range of the m^*_D/m values can be broader in the models which take into account the correlations beyond mean-field correlations.

(v) Particle-vibration coupling substantially improves the description of splitting energies in pseudospin doublets as compared with mean-field calculations. Observed similarity of the splitting energies of proton and neutron pseudospin doublets with the same single-particle structure in medium- and heavy-mass nuclei can only be reproduced when the particle-vibration coupling is taken into account.

(vi) The spherical shell closures in superheavy nuclei are still found at proton $Z = 120$ and neutron $N = 172$ numbers even when particle-vibration coupling is taken into account. However, the size of these gaps becomes

smaller (as compared with mean field values) in the presence of particle-vibration coupling due to general compression of the spectra caused by the increase of the effective mass of the nucleon at the Fermi level.

(vii) The NL3* parametrization employed in the current work has been adjusted at the mean-field level. The remaining discrepancies between the results of the particle vibration coupling model and experiment clearly suggest that this parametrization is not completely adequate for the description of the energies of the single-particle states. We believe that this statement is not limited to NL3* but is also valid for all existing CDFT parametrizations which have been adjusted at the mean-field level. This calls for the parametrizations specifically tailored to describe single-particle degrees of freedom in the models taking into account the correlations beyond mean field correlations.

ACKNOWLEDGMENTS

This work was supported by the LOEWE program of the State of Hesse (Helmholtz International Center for FAIR) and by the US Department of Energy under Grant No. DE-FG02-07ER41459.

[1] P.-G. Reinhard, Rep. Prog. Phys. **52**, 439 (1989).
[2] P. Ring, Prog. Part. Nucl. Phys. **37**, 193 (1996).
[3] D. Vretenar, A. V. Afanasjev, G. A. Lalazissis, and P. Ring, Phys. Rep. **409**, 101 (2005).
[4] M. Bender, K. Rutz, P.-G. Reinhard, J. A. Maruhn, and W. Greiner, Phys. Rev. C **60**, 034304 (1999).
[5] A. V. Afanasjev and H. Abusara, Phys. Rev. C **81**, 014309 (2010).
[6] J. N. Ginocchio, Phys. Rev. Lett. **78**, 436 (1997).
[7] U. Hofmann and P. Ring, Phys. Lett. B **214**, 307 (1988).
[8] A. V. Afanasjev, G. Lalazissis, and P. Ring, Nucl. Phys. A **634**, 395 (1998).
[9] A. V. Afanasjev, I. Ragnarsson, and P. Ring, Phys. Rev. C **59**, 3166 (1999).
[10] A. V. Afanasjev and P. Ring, Phys. Scr., T **88**, 10 (2000).
[11] A. V. Afanasjev and S. Frauendorf, Phys. Rev. C **71**, 064318 (2005).
[12] T. Bengtsson and I. Ragnarsson, Nucl. Phys. A **436**, 14 (1985).
[13] K. Rutz, M. Bender, P.-G. Reinhard, J. A. Maruhn, and W. Greiner, Nucl. Phys. A **634**, 67 (1998).
[14] P. Quentin and H. Flocard, Ann. Rev. Nucl. Part. Sci. **28**, 523 (1978).
[15] P. Ring and P. Schuck, *The Nuclear Many-body Problem* (Springer Verlag, Heidelberg, 1980).
[16] C. Mahaux, P. F. Bortignon, R. A. Broglia, and C. H. Dasso, Phys. Rep. **120**, 1 (1985).
[17] E. Litvinova and P. Ring, Phys. Rev. C **73**, 044328 (2006).
[18] S. Baroni, F. Barranco, P. F. Bortignon, R. A. Broglia, G. Colò, and E. Vigezzi, Phys. Rev. C **74**, 024305 (2006).
[19] V. G. Soloviev, *Theory of Complex Nuclei* (Pergamon, Oxford, 1976).
[20] V. G. Soloviev, *Theory of Atomic Nuclei: Quasiparticles and Phonons* (Institute of Physics Publishing, Bristol and Philadelphia, 1992).
[21] A. Bohr and B. R. Mottelson, *Nuclear Structure* (World Scientific, 1998), Vol. II.
[22] A. V. Afanasjev, T. L. Khoo, S. Frauendorf, G. A. Lalazissis, and I. Ahmad, Phys. Rev. C **67**, 024309 (2003).
[23] S. Shawaqfeh and A. V. Afanasjev (to be submitted to Phys. Rev. C).
[24] M. Jaminon and C. Mahaux, Phys. Rev. C **40**, 354 (1989).
[25] T. Nikšić, D. Vretenar, and P. Ring, Phys. Rev. C **78**, 034318 (2008).
[26] G. A. Lalazissis, J. König, and P. Ring, Phys. Rev. C **55**, 540 (1997).
[27] G. A. Lalazissis, S. Karatzikos, R. Fossion, D. Peña Arteaga, A. V. Afanasjev, and P. Ring, Phys. Lett. B **671**, 36 (2009).
[28] W. Koepf and P. Ring, Nucl. Phys. A **493**, 61 (1989).
[29] V. I. Isakov, K. I. Erokhina, H. Mach, M. Sanchez-Vega, and B. Fogelberg, Eur. Phys. J. A **14**, 29 (2002).
[30] L. Trache, A. Kolomiets, S. Shlomo, K. Heyde, H. Dejbakhsh, C. A. Gagliardi, R. E. Tribble, X. G. Zhou, V. E. Iacob, and A. M. Oros, Phys. Rev. C **54**, 2361 (1996).
[31] P. F. Bortignon, G. Coló, and H. Sagawa, J. Phys. G **37**, 064013 (2010).
[32] M. Baranger, Nucl. Phys. A **149**, 225 (1970).
[33] J. Dudek, B. Szpak, M.-G. Porguet, H. Molique, K. Rybak, and B. Fornal, J. Phys. G **37**, 064031 (2010).
[34] J. Lee, M. B. Tsang, W. G. Lynch, M. Horoi, and S. C. Su, Phys. Rev. C **79**, 054611 (2009).
[35] P. Grabmayr, A. Mondry, G. J. Wagner, P. Woldt, G. P. A. Berg, J. Lisantti, D. W. Miller, H. Nann, P. P. Singh, and E. J. Stephenson, J. Phys. G **18**, 1743 (1992).
[36] S. Gales, C. P. Massolo, S. Fortier, J. P. Schapira, P. Martin, and V. Comparat, Phys. Rev. C **31**, 94 (1985).
[37] S. Gales, G. M. Crawley, D. Weber, and B. Zwieglinski, Phys. Rev. **18**, 2475 (1978).
[38] H. Langevin-Joliot *et al.*, Phys. Rev. **47**, 1571 (1993).
[39] J. König and P. Ring, Phys. Rev. Lett. **71**, 3079 (1993).
[40] A. V. Afanasjev, J. König, and P. Ring, Nucl. Phys. A **608**, 107 (1996).
[41] A. V. Afanasjev and H. Abusara, Phys. Rev. C **82**, 034329 (2010).
[42] M. Anguiano, J. L. Egido, and L. M. Robledo, Phys. Lett. B **545**, 62 (2002).
[43] A. V. Afanasjev, P. Ring, and J. König, Nucl. Phys. A **676**, 196 (2000).
[44] A. Bohr and B. Mottelson, *Nuclear Structure* (Benjamin, New York, 1975), Vol. II.
[45] A. B. Migdal, *Theory of Finite Fermi Systems and Properties of Atomic Nuclei*, 2nd ed. (Nauka, Moscow, 1983).
[46] P. Ring, Zhong-yu Ma, Nguen Van Giai, D. Vretenar, A. Wandelt, and Li-Gang Cao, Nucl. Phys. A **694**, 249 (2001).
[47] E. Litvinova, P. Ring, and V. I. Tselyaev, Phys. Rev. C **78**, 014312 (2008).
[48] E. Litvinova, P. Ring, and V. Tselyaev, Phys. Rev. C **75**, 064308 (2007).
[49] Z. Q. Sheng, Z. Z. Ren, and W. Z. Hang, Nucl. Phys. A **832**, 49 (2010).

[50] H. Abusara, A. V. Afanasjev, and P. Ring, Phys. Rev. C **82**, 044303 (2010).
[51] T. Gaitanos, A. B. Larionov, H. Lenske, and U. Mosel, Phys. Rev. C **81**, 054316 (2010).
[52] G. Coló, H. Sagawa, and P. F. Bortignon, Phys. Rev. C **82**, 064307 (2010).
[53] D. Seweryniak *et al.*, Phys. Rev. Lett. **99**, 022504 (2007).
[54] I. G. Darby *et al.*, Phys. Rev. Lett. **105**, 162502 (2010).
[55] H. Grawe, R. Schubart, K. H. Maier, and D. Seweryniak, Phys. Scr., T **56**, 71 (1995).
[56] O. V. Bespalova, I. N. Boboshin, V. V. Varlamov, T. A. Ermakova, B. S. Ishkhanov, E. A. Romanovskii, T. I. Spasskaya, and T. P. Timokhina, Bull. Russ. Acad. Sc. **71**, 434 (2007).
[57] C. Ellegaard and P. Vedelsby, Phys. Lett. B **26**, 155 (1968).
[58] P. D. Barnes, E. R. Flynn, G. J. Igo, and D. D. Armstrong, Phys. Rev. C **1**, 228 (1970).
[59] R. A. Moyer, B. L. Cohen, and R. C. Diehl, Phys. Rev. C **2**, 1898 (1970).
[60] J. Guillot, J. Van de Wiele, H. Langevin-Joliot, E. Gerlic, J. P. Didelez, G. Duhamel, G. Perrin, M. Buenerd, and J. Chauvin, Phys. Rev. C **21**, 879 (1980).
[61] C. Ellegaard, J. Kantele, and P. Vedelsby, Nucl. Phys. A **129**, 113 (1969).
[62] R. Tickle and W. S. Gray, Nucl. Phys. A **247**, 187 (1975).
[63] K. L. Jones *et al.*, Nature (London) **465**, 454 (2010).
[64] K. L. Yurkewicz *et al.*, Phys. Rev. C **74**, 024304 (2006).
[65] C. Barbieri, Phys. Rev. Lett. **103**, 202502 (2009).
[66] K. T. Hecht and A. Adler, Nucl. Phys. A **137**, 129 (1969).
[67] A. Arima, M. Harvey, and K. Shimizu, Phys. Lett. B **30**, 517 (1969).
[68] J. N. Ginocchio, Phys. Rep. **414**, 165 (2005).
[69] Huo Junde, Nucl. Data Sheets **64**, 723 (1991).
[70] M. R. Bhat, Nucl. Data Sheets **85**, 415 (1998).
[71] B. Fogelberg *et al.*, Phys. Rev. C **70**, 034312 (2004).
[72] Yu. Khazov, I. Mitropolsky, A. Rodionov, Nucl. Data Sheets **107**, 2715 (2006).
[73] W. Urban, A. Zlomaniec, G. S. Simpson, H. Faust, T. Rzkaca-Urban, and M. Jentschel, Phys. Rev. C **79**, 037304 (2009).
[74] M. Sanchez-Vega, B. Fogelberg, H. Mach, R. B. E. Taylor, A. Lindroth, J. Blomqvist, A. Covello, and A. Gargano, Phys. Rev. C **60**, 024303 (1999).
[75] M. J. Martin, Nucl. Data Sheets **63**, 723 (1991).
[76] M. J. Martin, Nucl. Data Sheets **70**, 315 (1993).
[77] G. Audi, A. H. Wapstra, and C. Thibault, Nucl. Phys. A **729**, 337 (2003).
[78] Huo Junde, Nucl. Data Sheets **109,** 787 (2008).